metals

MDPI

Article

Constitutive Modeling and Fracture Characteristics of Die-Cast Mg-7Al-1.5La-1Zn Alloy Under Complex Stress States for Vehicle Crash Simulation

Jinsheng Zhang [1,2], Guangsheng Huang [1,*], Sha Lan [1,2], Jian Yang [3], Jie Zhang [2], Ping Chen [2], Yazhou Jiang [2], Yunyun Wang [2], Qin Yang [2] and Bo Liu [3,*]

[1] College of Materials Science and Engineering, Chongqing University, No. 174, Shazheng Street, Shapingba District, Chongqing 400044, China; zhangjs2@changan.com.cn (J.Z.)
[2] Global R&D Center, Chongqing Changan Automobile Co., Ltd., Chongqing 401120, China
[3] School of Mechanical Engineering, University of Science and Technology Beijing, Beijing 100083, China
* Correspondence: gshuang@cqu.edu.cn (G.H.); liubo1@ustb.edu.cn (B.L.)

Abstract

To support vehicle crash simulation in lightweight automotive design, this study develops high-precision constitutive and fracture models for a giga casting Mg-7Al-1.5La-1Zn magnesium alloy. Through mechanical testing and microstructural analysis, the plastic hardening, strain-rate strengthening, and ductile fracture behaviors are systematically investigated. A weighted mixed hardening model combining the saturation-type Hockett–Sherby and unsaturated Swift models is established. To overcome the limitations of the classical Johnson–Cook (J-C) model in capturing strain rate–plastic strain coupling, a modified dynamic increase factor incorporating equivalent plastic strain is proposed. Comparative fitting with the Cowper–Symonds model confirms that the modified J-C model better captures the twinning deformation mechanism under high strain rates and achieves higher accuracy. Among three fracture models Johnson–Cook (J-C), Modified Mohr-Coulomb(MMC), and Damage Initiation and Evolution Model (DIEM), the MMC model, which incorporates both stress triaxiality and Lode angle, shows the best predictive performance, with an average accuracy of 86.46% for fracture displacement across the full stress range. Microstructural characterization reveals grain refinement and dispersed $Al_{11}La_3$ precipitates that improve grain boundary properties. The established parameter set and calibration methods provide a reliable reference for material card calibration in crash simulation of giga casting magnesium alloy body structures.

Keywords: lightweight; magnesium alloy; plastic constitutive model; fracture model

Check for updates

Academic Editor: Alberto Campagnolo

Received: 13 June 2026
Revised: 6 July 2026
Accepted: 9 July 2026
Published: 12 July 2026

Copyright: © 2026 by the authors. Licensee MDPI, Basel, Switzerland. This article is an open access article distributed under the terms and conditions of the Creative Commons Attribution (CC BY) license.

1. Introduction

To achieve global carbon emission reduction targets, the transportation sector has continuously promoted vehicle lightweighting [1]. According to the Energy-saving and New Energy Vehicle Roadmap released by the China Society of Automotive Engineers, a 100 kg reduction in vehicle curb mass can reduce the energy consumption of battery electric vehicles by 0.4–0.5 kWh/100 km [2]. Vehicle lightweighting is mainly realized through structural optimization and the adoption of lightweight materials, which include ultra-high-strength steel, aluminum alloy, magnesium alloy and composite materials. Magnesium alloy has a density of 1.74 g/cm^3. It features higher specific strength and specific stiffness than steel and aluminum alloys, and is far superior to engineering plastics. As

the lightest structural metallic material available today, magnesium alloy can reduce the weight of vehicle body structures by approximately 40% compared with steel structures and by 20% compared with aluminum structures, as reported by Stephen Logan and other researchers [3–6]. With rising aluminum prices and decreasing magnesium prices, major Chinese automotive manufacturers have initiated extensive research and industrial applications. For instance, Changan Automobile has developed distributed magnesium alloy electric drive housings; Seres Auto in Chongqing has adopted magnesium alloys for rear floor panels; and FAW Group has developed magnesium alloy seat frames and inner tailgate panels [7–9]. Despite these advances, existing studies have predominantly focused on novel magnesium alloy material development and casting process optimization. When magnesium alloys are employed in automotive structural components, they are generally subjected to complex stress states involving combined tension, compression, and shear during vehicle collisions. However, research on constitutive models tailored for automotive crashworthiness simulations remains limited, which restricts the broader application of magnesium alloys in load-bearing structural components.

Current research on constitutive models for magnesium alloys primarily follows two main directions: macroscopic phenomenological models and microstructural-mechanism-based crystal plasticity models. In engineering practice, macroscopic phenomenological approaches dominate due to their high computational efficiency and relatively straightforward parameter calibration. The widely adopted macroscopic phenomenological models include the Johnson–Cook (J-C) model [10], the Modified Mohr–Coulomb (MMC) fracture model [11], the Damage Initiation and Evolution Model (DIEM) [12], the Arrhenius-type model, and the Fields–Backofen model. Among these, J-C, MMC, and DIEM are the most extensively used constitutive frameworks for metallic materials in the automotive engineering domain. Chen et al. [13] investigated the plastic deformation constitutive behavior of AZ80 alloy through multiple isothermal uniaxial hot compression tests at four temperatures and strain rates ranging from 0.001 s^{-1} to 1 s^{-1}, employing a modified Arrhenius relationship to describe the pre-peak strain behavior and a modified J-C model for the post-peak stage. Mirza et al. [14] established a modified J-C equation to predict the flow stress of the extruded rare-earth magnesium alloy Mg-10Gd-3Y-0.5Zr based solely on compression tests (strain rates from 0.0001 s^{-1} to 0.1 s^{-1}), achieving a prediction standard deviation of approximately 1.8%. Li et al. [15] conducted uniaxial tension tests at various strain rates and proposed a rate-dependent M-J-C model to predict the plasticity and fracture behavior of AZ31B magnesium alloy. Chang et al. [16] investigated the constitutive models for AZ80 magnesium alloy under compression at different loading directions and strain rates, and found that the log-M linear model provides higher accuracy than the modified Johnson–Cook model. Solanki et al. [17] elucidated the complex interplay among stress triaxiality, deformation rate, and microstructural mechanisms, revealing that loading rate and stress state significantly influence deformation behavior: quasi-static loading tends to induce twin–twin interactions, whereas dynamic loading at high strain rates predominantly triggers detwinning as the dominant mechanism.

Existing studies indicate that magnesium alloys exhibit sustained work hardening accompanied by a progressively decreasing hardening rate at large strains. The Swift (power-law) model and the Hockett–Sherby (saturation-exponential) model describe this behavior from different perspectives; however, no single model achieves optimal fitting accuracy across the full strain range. Sami [18] investigated the mechanical properties and numerical simulation of Mg-ZM51M magnesium alloy. Liu et al. [19] proposed an improved J-C model to eliminate the prediction limitations of the conventional model at high temperatures and high strain rates. Yang et al. [20] proposed a global optimization

method for magnesium alloys based on multi-stress-state experiments, overcoming the limitations of conventional uniaxial tension data extrapolation.

Current research on magnesium alloy constitutive modeling suffers from three major deficiencies: (1) Most existing constitutive studies are confined to simple stress states such as uniaxial tension, uniaxial compression, or elevated-temperature tension. In contrast, real service conditions such as automotive crashes involve multiaxial stress states, and models calibrated under single stress states cannot accurately capture deformation behavior [21]. (2) Most studies focus on wrought magnesium alloys (extruded or rolled), while constitutive modeling of cast magnesium alloys, particularly high-pressure die casting alloys used in automotive applications, remains insufficient. Cast magnesium alloys exhibit a random grain orientation distribution and near-isotropic characteristics, with hardening behavior fundamentally different from that of wrought alloys. (3) The extrapolation accuracy of different hardening models under large-strain conditions varies considerably. Nevertheless, systematic comparative assessments of various hardening models across a wide strain range and under multiple stress states are lacking in the magnesium alloy literature. For instance, the J-C model intrinsically decouples strain hardening, strain-rate strengthening, and thermal softening, making it difficult to accurately describe the complex strain-hardening evolution of magnesium alloys, especially the hardening behavior at large strains [22].

In view of the above limitations, this study investigates a self-developed giga casting Mg-7Al-1.5La-1Zn magnesium alloy. A weighted mixed hardening constitutive equation is established by combining the saturation-type Hockett–Sherby and the non-saturated Swift hardening models. To overcome the deficiency of the classical J-C model in which the strain-rate term fails to capture the coupling between plastic strain and strain-rate sensitivity, a modified dynamic increase factor (DIF) coupled with a power term of equivalent plastic strain is proposed. The fitting accuracies of the modified J-C model and the Cowper–Symonds strain-rate model are compared, demonstrating that the modified J-C model better accommodates the twinning deformation mechanism of magnesium alloys at high strain rates and achieves superior fitting precision. Furthermore, fracture prediction capabilities of J-C, MMC, and DIEM are systematically evaluated across a full stress triaxiality range from pure shear to high tension, with mesh convergence analysis performed. The MMC fracture model, which accounts for both stress triaxiality and Lode angle, delivers an average prediction accuracy of 86.46% for fracture displacement across the full stress range, outperforming the J-C and DIEM. Microstructural characterization reveals grain refinement and a dispersed distribution of rare-earth $Al_{11}La_3$ precipitates, which effectively optimize grain boundary properties. The complete set of high-precision constitutive parameters, fracture parameters, and mesh calibration methods established in this paper provides a theoretical foundation and engineering reference for the accurate calibration of material cards used in crash simulation of giga casting magnesium alloy body structures.

2. Materials and Methods

The magnesium alloy investigated in this study is an independently developed material with a chemical composition of Mg-7Al-1.5La-1Zn (see Table 1 for detailed composition). The alloy was cast into slab blanks with dimensions of 200 mm × 180 mm × 3.5 mm, which were then cut and machined as required. The main casting process parameters were set as follows: molten alloy temperature of 670 °C, mold temperature of 200 °C, and applied pressure of 30 MPa.

Table 1. Chemical composition of Mg-7Al-1.5La-1Zn (wt %).

Alloy Designation	Al	La	Zn	Mn	Mg
AE715 (Mg-7Al-1.5La-1Zn)	6.5–7.5	1.0–1.5	0.9–1.1	0.2–0.4	Bal.
Measured composition	6.84	1.41	1.02	0.34	Bal.

As shown in Figure 1, seven types of characteristic specimens were designed, including quasi-static uniaxial tension, high-speed uniaxial tension, pure shear, tension–shear combination, R20 notched tension, R5 notched tension and central hole tension. These specimens cover the typical stress states encountered in vehicle collision conditions. The stress triaxiality of pure shear specimens is 0, that of uniaxial tension specimens is 0.33, R20 notched tension specimens is 0.45, R5 notched tension specimens is 0.74, and central hole specimens is 0.5 [23].

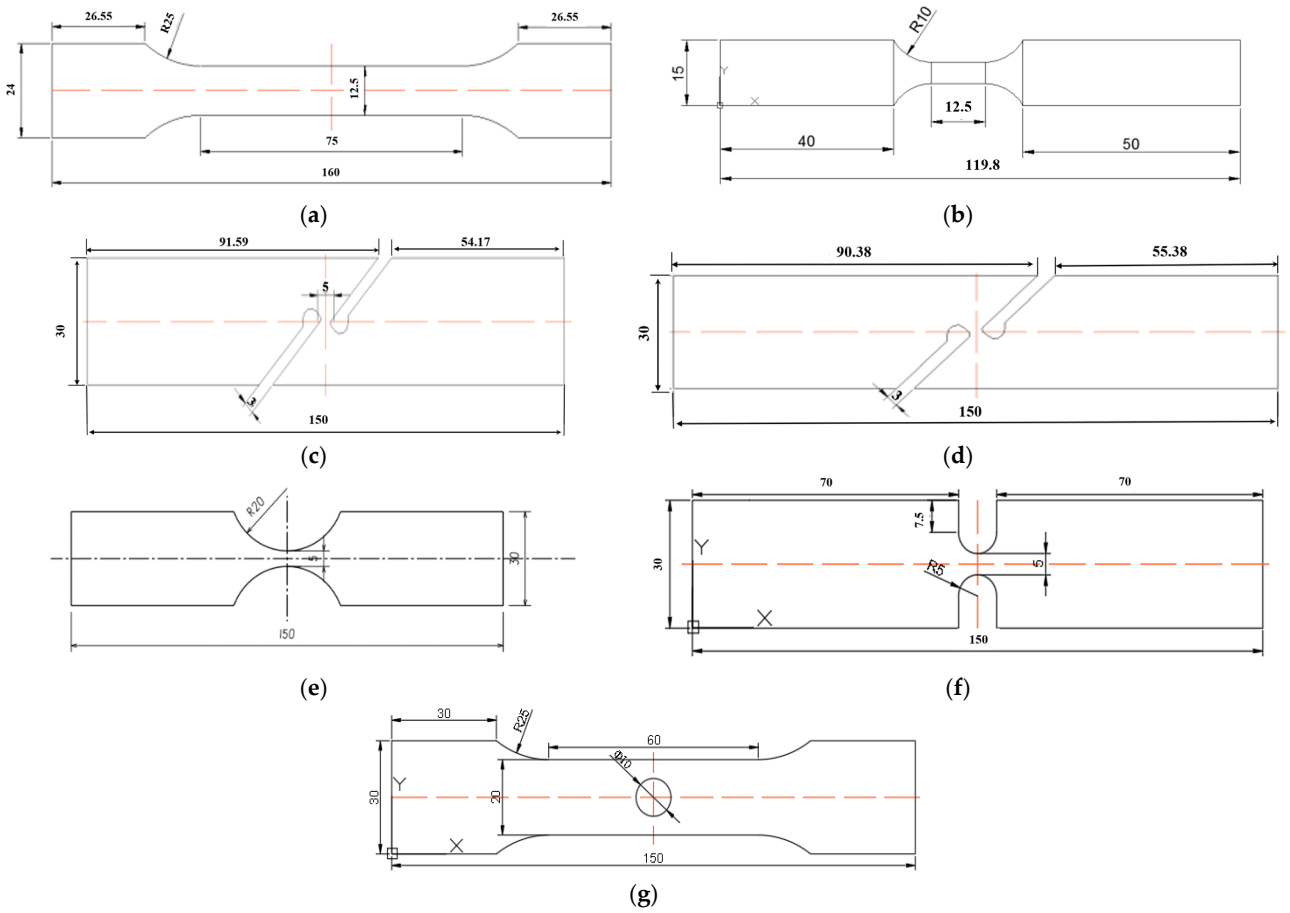

Figure 1. Specimens for mechanical tests of cast magnesium alloy. (**a**) Quasi-static tension specimen, (**b**) high-speed tension specimen, (**c**) pure shear specimen, (**d**) tension–shear specimen, (**e**) R20 notched tension specimen, (**f**) R5 notched tension specimen, (**g**) central hole specimen. (unit: mm).

As shown in Figure 2, uniaxial and notched tensile specimens were tested using a CMT5305 electronic universal testing machine (MTS Systems (China) Co., Ltd., Jinan, China) combined with a non-contact digital image correlation (DIC) system, and the force–displacement curves under quasi-static conditions were obtained. Dynamic tensile tests were carried out on a Zwick HTM5020 high-speed tensile testing machine (ZwickRoell GmbH & Co. KG, Ulm, Germany) at five strain rates of 0.001/s, 0.1/s, 10/s, 100/s and 500/s to obtain force–displacement curves at different strain rates.

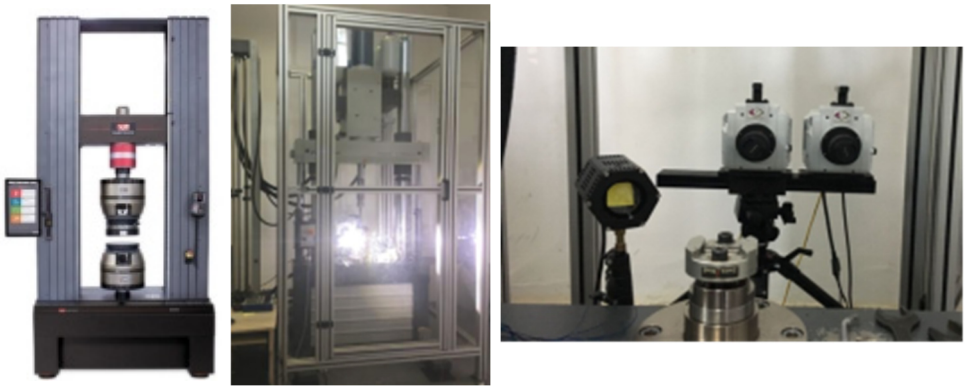

(**a**) (**b**) (**c**)

Figure 2. Test equipment. (**a**) CMT5305 electronic universal testing machine, (**b**) high-speed tensile testing machine, (**c**) full-strain field measurement system.

The quasi-static tensile tests, shear tests and R10 notched tensile tests were conducted in accordance with GB/T 228.1 [24], while high-speed tensile tests followed ISO 26203-2 [25]. All tests were repeated no less than three times. Load data were collected by the testing machine, and digital images were captured via the DIC system. Surface displacement fields were calculated using post-processing software by tracking identical speckles in the stochastic speckle patterns.

Specimens were cut from the as-cast magnesium alloy plate matrix. After sampling, optical microscopy (OM) was adopted to observe the cross-sectional morphology of the specimens. For metallographic sample preparation, the specimens were mechanically ground step by step with SiC abrasive papers ranging from 200# to 2000# grit size, followed by etching in picric acid solution (0.85 g picric acid, 2 mL glacial acetic acid, 2 mL anhydrous ethanol and 10 mL distilled water) for 10 s. A ZEISS Axiovert 40 MAT optical microscope (Carl Zeiss AG, Oberkochen, Germany) was finally used to characterize the microstructure of the alloy.

Fracture morphologies of specimens after quasi-static and high-speed tensile tests were observed using an Oxford Ultim Max 60 scanning electron microscope (SEM) (Oxford Instruments NanoAnalysis, High Wycombe, UK). Fracture observation was performed immediately after testing. Appropriate protection measures were adopted during sampling to prevent oxidation and contamination of fracture surfaces, which may otherwise have affected the observation results. Additionally, magnesium alloy chips were cut from the specimens for X-ray diffraction (XRD) characterization using a D/max−2500PC X-ray diffractometer (Rigaku Corporation, Tokyo, Japan). Cu Kα radiation was used for XRD analysis at an operating current of 40 mA and an applied voltage of 40 kV. The scanning range was set from 10° to 80° at a scanning speed of 2°/min. All test data processing and plotting were completed using Origin 9.0 (OriginLab Corporation, Northampton, MA, USA). The constitutive model analysis and crash simulation were carried out via LS-DYNA R11.0 (LSTC, Livermore, CA, USA).

As shown in Table 2, quasi-static tests were implemented for constitutive model research, and dynamic tests were conducted to analyze the strain-rate effect. Three specimens were tested for each test condition.

Table 2. Test types and experimental conditions.

Type	Strain Rate (/s)	Specimen Quantity	Test Purpose
Quasi-static	0.001	5 × 3	Constitutive parameters
Dynamic	1/10/100/500	5 × 3	Strain-rate effect

3. Results

In the crash simulation of automotive magnesium alloy structural components, it is essential to establish constitutive models and ductile fracture models for magnesium alloys. Constitutive models characterize elastic behavior, plastic hardening, strain-rate effects, and temperature-dependent flow behavior, and quantitatively describe the intrinsic stress–strain relationships under various loading conditions, serving as the fundamental basis for mechanical calculations [26]. Combined with state parameters such as stress triaxiality and Lode angle, the fracture model depicts the whole process of damage initiation, evolution and ductile fracture, and defines the critical failure conditions of materials.

As shown in Figure 3, the coupled constitutive–fracture framework can effectively reveal the deformation and failure mechanisms of magnesium alloys under complex loading conditions, including impact, tension, and shear. This study improves crash simulation accuracy and provides important theoretical support for structural optimization, service reliability assessment, and engineering applications of giga casting magnesium alloy components.

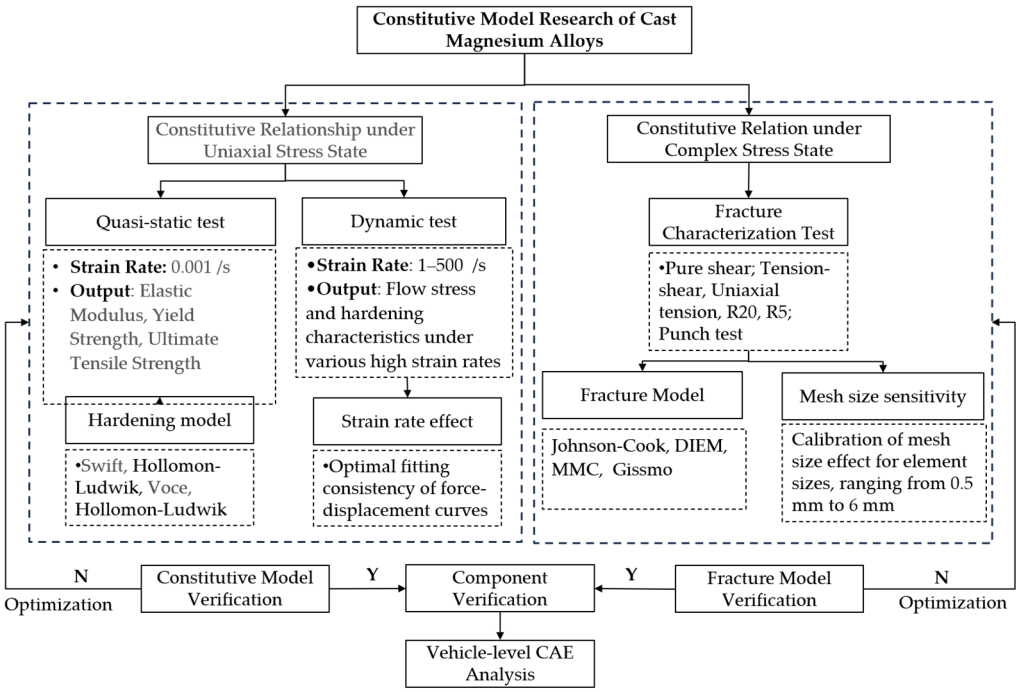

Figure 3. Calibration process of material models for crash simulation of giga casting magnesium alloy.

3.1. Basic Mechanical Property Tests

Quasi-static and high-speed tensile tests were conducted on the giga casting magnesium alloy. As shown in Figure 4a, the alloy exhibits a yield strength of 147.3 MPa, an ultimate tensile strength of 276.1 MPa and an elongation of 12.8%. After necking, no obvious localized deformation is observed, and the specimen fractures rapidly. High-speed tensile tests were performed at five strain rates: 0.001/s, 1/s, 10/s, 100/s and 500/s, and the results are presented in Figure 4b. The test results indicate that the yield strength increases with the rising strain rate, proving that the material has strain-rate sensitivity at a moderate level. Meanwhile, the alloy maintains a relatively high fracture strain under high strain rates, which means it possesses excellent energy absorption capacity under high-speed crash conditions.

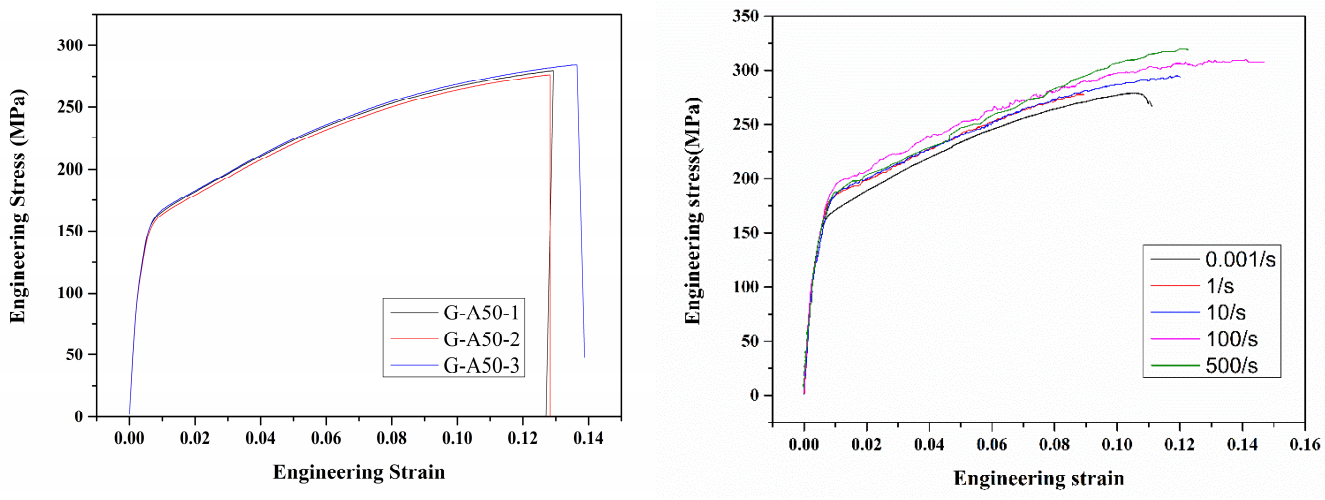

(**a**) (**b**)

Figure 4. Engineering stress–engineering strain curve of the giga casting magnesium alloy sheet. (**a**) Quasi-static tension, (**b**) dynamic tension.

3.2. Fracture Property Tests

When the giga casting magnesium alloy is applied to automotive rear floors, it needs to withstand complex service conditions such as side-pillar collision and rear-end collision. To investigate its fracture properties under diverse stress states, tests were carried out on pure shear, tension–shear, R20/R5 notched tension and central hole specimens. As shown in Figure 5, all specimens under the four stress states fractured rapidly after the load reached the peak value, with no obvious localized deformation prior to fracture.

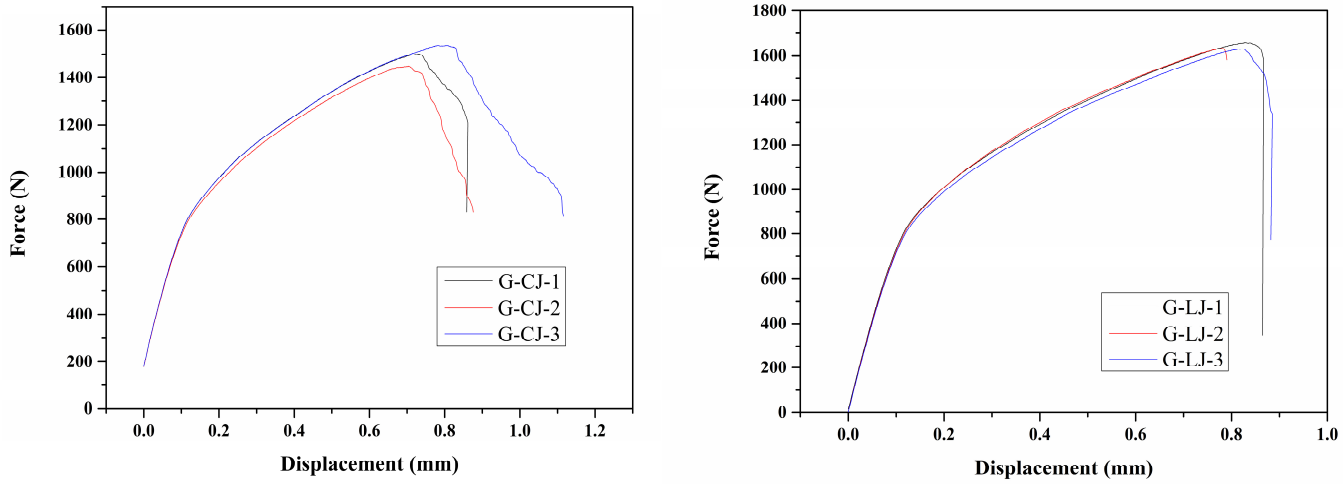

(**a**) (**b**)

Figure 5. *Cont.*

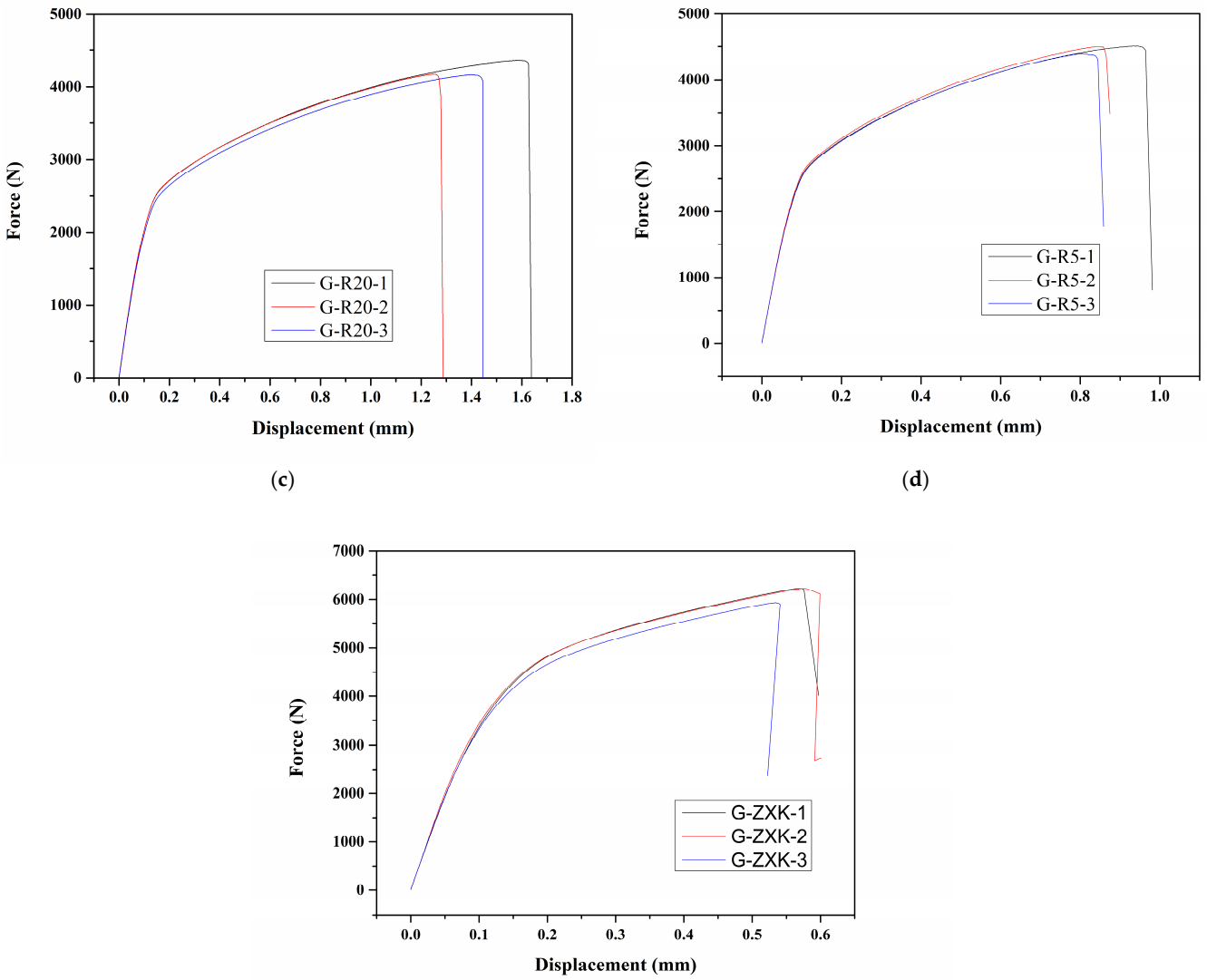

Figure 5. Test results under different stress states. (**a**) Pure shear, (**b**) tension–shear, (**c**) R20 notched tension, (**d**) R5 notched tension, (**e**) central hole test.

4. Study on Plastic Constitutive Model

A mechanical constitutive model consists of a yield criterion and hardening criterion. The yield criterion determines when the material reaches the yield surface, while the hardening criterion describes the evolution of the yield locus during deformation. To balance computational efficiency and predictive accuracy, isotropic constitutive models are widely adopted in the automotive industry for simulating the deformation behavior of magnesium alloy components. Accordingly, this study adopts the von Mises yield criterion and an isotropic constitutive framework to investigate the plastic constitutive behavior of the giga casting magnesium alloy.

4.1. Constitutive Relationship Under Uniaxial Stress

Based on the force–displacement curves obtained from tensile tests, engineering stress is calculated by dividing the load by the cross-sectional area of the specimen's parallel section, and engineering strain is derived from the displacement divided by the gauge length. The true stress and true strain are calculated via Formulas (1) and (2), and the plastic strain is obtained using Formula (3) [27]. Figure 6 presents the true stress–true strain curve and true stress–plastic strain curve of the magnesium alloy. The true stress–true strain curve

eliminates errors caused by geometric changes under large deformation and accurately reflects the intrinsic mechanical properties of the material. Covering both elastic and plastic deformation stages, it serves as the foundation for establishing constitutive models. The true stress–plastic strain curve excludes elastic strain and retains only plastic deformation information, enabling precise characterization of work-hardening behavior and making it suitable for hardening model extrapolation. Both curves share identical true stress values, while the total true strain is the sum of the elastic and plastic strain components. In finite element modeling of magnesium alloys, the true stress–plastic strain data are generally used to fit hardening equations, while the true stress–true strain curve is applied to analyze overall deformation characteristics. This approach ensures high accuracy in parameter calibration for constitutive and fracture models.

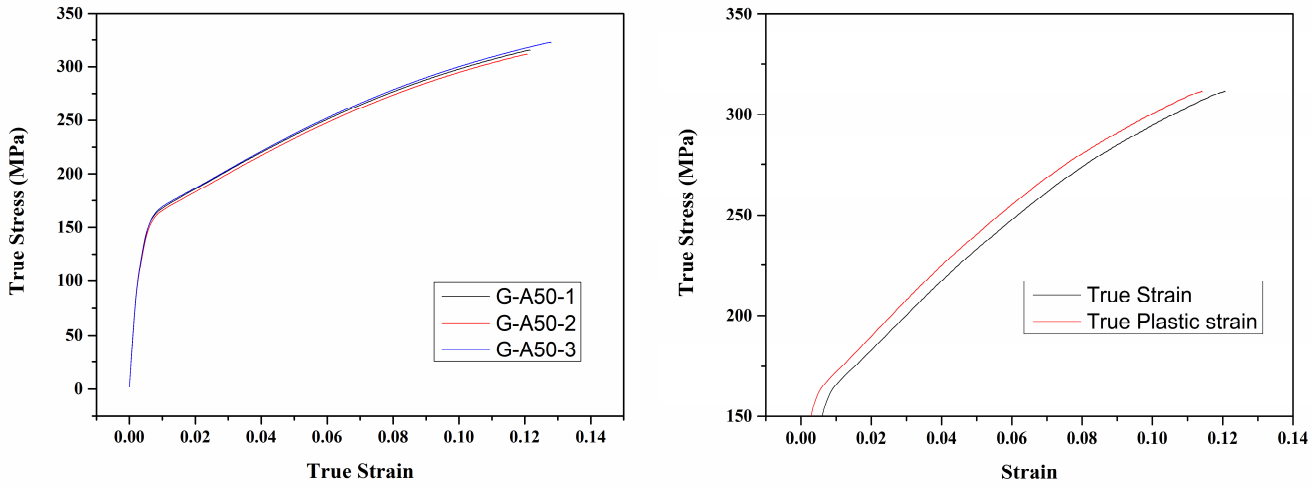

(**a**) (**b**)

Figure 6. True stress–strain curves and true plastic strain curves of giga casting magnesium alloy. (**a**) True stress–true strain curve, (**b**) curves of true stress–true strain and true stress–plastic strain.

Calculation of true stress:

$$\sigma_T = \sigma(1 + \varepsilon) \quad (1)$$

Calculation of true strain:

$$\varepsilon_T = \ln(1 + \varepsilon) \quad (2)$$

where σ and ε denote engineering stress and engineering strain, respectively.

Calculation of plastic strain:

$$\varepsilon_p = \ln(1 + \varepsilon_T - \frac{\sigma}{E}) \quad (3)$$

where ε_p is plastic strain, ε_T is true strain, σ is engineering stress, and E is elastic modulus.

To accurately predict the large deformation behavior of automotive giga casting magnesium alloy components in service, hardening models are required to extrapolate the true stress–plastic strain curves. For metallic materials, commonly used hardening models are divided into non-saturated models and saturated models.

The non-saturated model, also known as the unbounded model, features continuously increasing stress with rising plastic strain without an upper limit, meaning hardening never terminates. Typical non-saturated models include the Swift model [28] and Hollomon–Ludwik model [29].

For saturated models, the flow stress gradually stabilizes at a constant saturation stress σ_{sat} after the plastic strain reaches a certain level, and work hardening ceases eventually.

Representative saturated models are the Hockett–Sherby model and Voce model. Obvious differences exist among the true stress–plastic strain curves fitted by different hardening models, as shown in Figure 7.

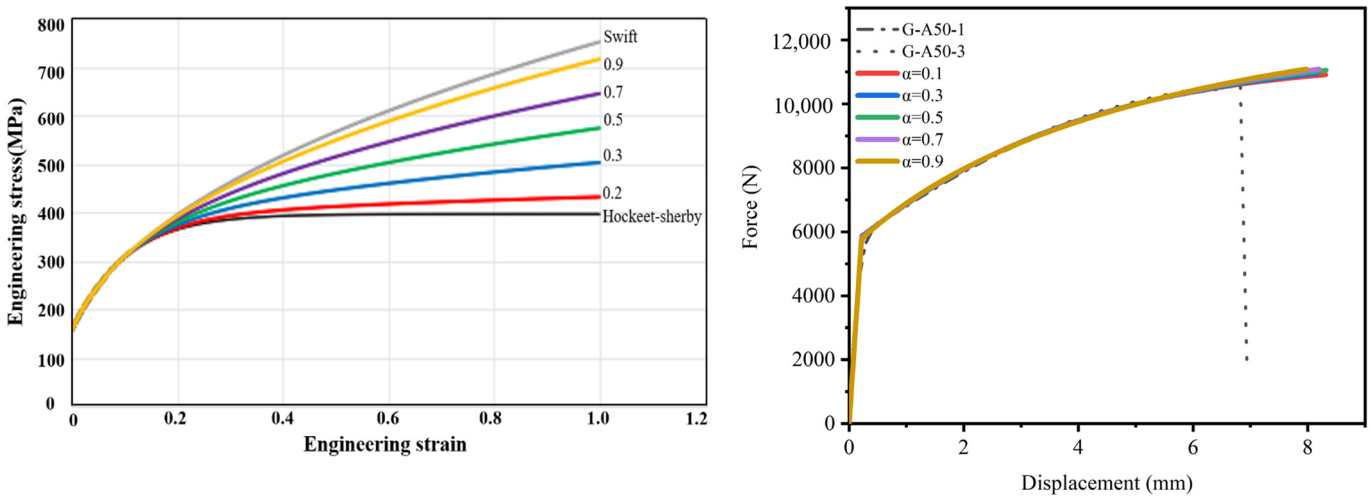

(**a**) (**b**)

Figure 7. Hardening model with different weighting coefficients. (**a**) Engineering stress–strain curves under different α; (**b**) engineering force–displacement curves under different α.

Swift constitutive equation:

$$\sigma_T = K(\varepsilon_p + \varepsilon_0)^n \quad (4)$$

σ_T : True stress; K: strength coefficient (hardening coefficient); ε_p: equivalent plastic strain; ε_0: initial plastic strain (offset strain); and n: material constant.

Hockett–Sherby constitutive equation

$$\sigma_T = \sigma_0 + A\left[1 - \exp\left(-b\varepsilon_p^m\right)\right] \quad (5)$$

σ_T : True stress; σ_0: initial yield stress; A is the saturation hardening amplitude; b is the hardening rate coefficient; ε_p^m: equivalent plastic strain; and m is the strain-hardening exponent.

Based on the isotropic mechanical behavior of giga casting magnesium alloy components, a weighted hardening model (Equation (6)) is adopted. This model combines the non-saturating Swift model and the saturation-type Hockett–Sherby model to extrapolate true stress–plastic strain curves and reproduce the actual deformation behavior of components. The weighting coefficient α satisfies $0 < \alpha < 1$. As presented in Figure 7, various extrapolated true stress–plastic strain curves and force–displacement curves are obtained by assigning different values to the weighting coefficient.

$$\sigma_T = \alpha \cdot K(\varepsilon_p + \varepsilon_0)^n + (1 - \alpha) \cdot \left[\sigma_0 + A\left[1 - \exp\left(-b\varepsilon_p^m\right)\right]\right] \quad (6)$$

Multiple groups of parallel uniaxial tensile specimens are fabricated and tested to obtain experimental peak forces. Finite element simulations are performed with different weighting coefficients α to extract simulated peak forces. The prediction accuracy of each single specimen is calculated by comparing the simulated peak force with the experimental counterpart. The accuracy values of all parallel tensile samples under the same α are averaged to acquire the average peak force accuracy under uniaxial stress corresponding to this weighting coefficient. The weighting coefficient α ranges from 0.1 to 0.9 at an

interval of 0.2, covering five values: 0.1, 0.3, 0.5, 0.7 and 0.9. This coefficient adjusts the contribution ratio of the Swift hardening term and the Hockett–Sherby hardening term in the coupled constitutive equation. Simulations are conducted sequentially for each set of α. The force–displacement curves and peak force data under all loading conditions are exported via LS-DYNA. The overall mean absolute accuracy covering six stress states is calculated, and the optimal weighting coefficient α applicable to uniaxial stress states is finally determined. For multiaxial stress states, six types of specimen models are established, including pure shear, tension–shear, uniaxial tension, R20 notched, R5 notched and central holed specimens. The accuracy analysis procedure is similar to that of uniaxial tension.

As shown in Table 3, when the weighting coefficient α is 0.3, the fitting accuracy of the average simulated force under uniaxial stress reaches a peak of 99.71%, which is the optimal result within the range of the parameters in this group. Among them, parameter K is 770, ε_0 is 0.0235, n is 0.4221, σ_0 is 146.3, A is = 658,754, b is 0.0011, and m is 0.6254. This high-precision fitting indicates that the flow-hardening behavior of the giga casting magnesium alloy during loading is more consistent with the theoretical characteristics of the saturated hardening model. With this weighting coefficient, the force–displacement curve output by the model shows the best agreement with the experimentally measured curve, verifying that the saturated hardening model can accurately characterize the plastic hardening evolution of the giga casting magnesium alloy under quasi-static and dynamic loads.

Table 3. Accuracy of average maximum force under uniaxial stress.

Hybrid Model	Maximum Force Accuracy (%)			
	Test-1	Test-2	Test-3	Average Absolute Accuracy
$\alpha = 0.1$	99.46	99.87	99.73	99.69 ± 0.21
$\alpha = 0.3$	99.28	99.87	99.99	99.71 ± 0.38
$\alpha = 0.5$	99.08	99.86	99.75	99.56 ± 0.42
$\alpha = 0.7$	98.9	99.86	99.49	99.42 ± 0.48
$\alpha = 0.9$	98.71	99.86	99.23	99.27 ± 0.57

4.2. Study on Constitutive Relation Under Complex Stress

Magnesium alloy components are generally subjected to combined tension–compression and shear loads with complex stress states during vehicle crash and impact events. Dynamic variations in stress triaxiality and Lode angle significantly affect the hardening response and fracture behavior of the material [30]. Conventional classical hardening models established under a single stress state fail to accurately characterize the nonlinear plastic evolution of materials. Accordingly, research on material constitutive relations under complex stress conditions is of great theoretical and engineering significance. Based on plastic flow theory, this study introduces a variable weighting coefficient to optimize a hybrid hardening criterion, coupling the effects of stress state parameters on hardening rate, plastic deformation, and damage evolution. It effectively addresses the limitation of traditional models that cannot adapt to complex stress states under multiple working conditions.

As shown in Figure 8, for the hybrid hardening models with different weighting coefficients under complex stress states, the weighting coefficient of the isotropic hardening model is defined as a function of stress triaxiality and Lode angle. This approach realizes the continuous transition of hardening behavior from tension to shear and from low to high multiaxial loading, and greatly improves the simulation accuracy of magnesium alloys under complex working conditions such as vehicle crash.

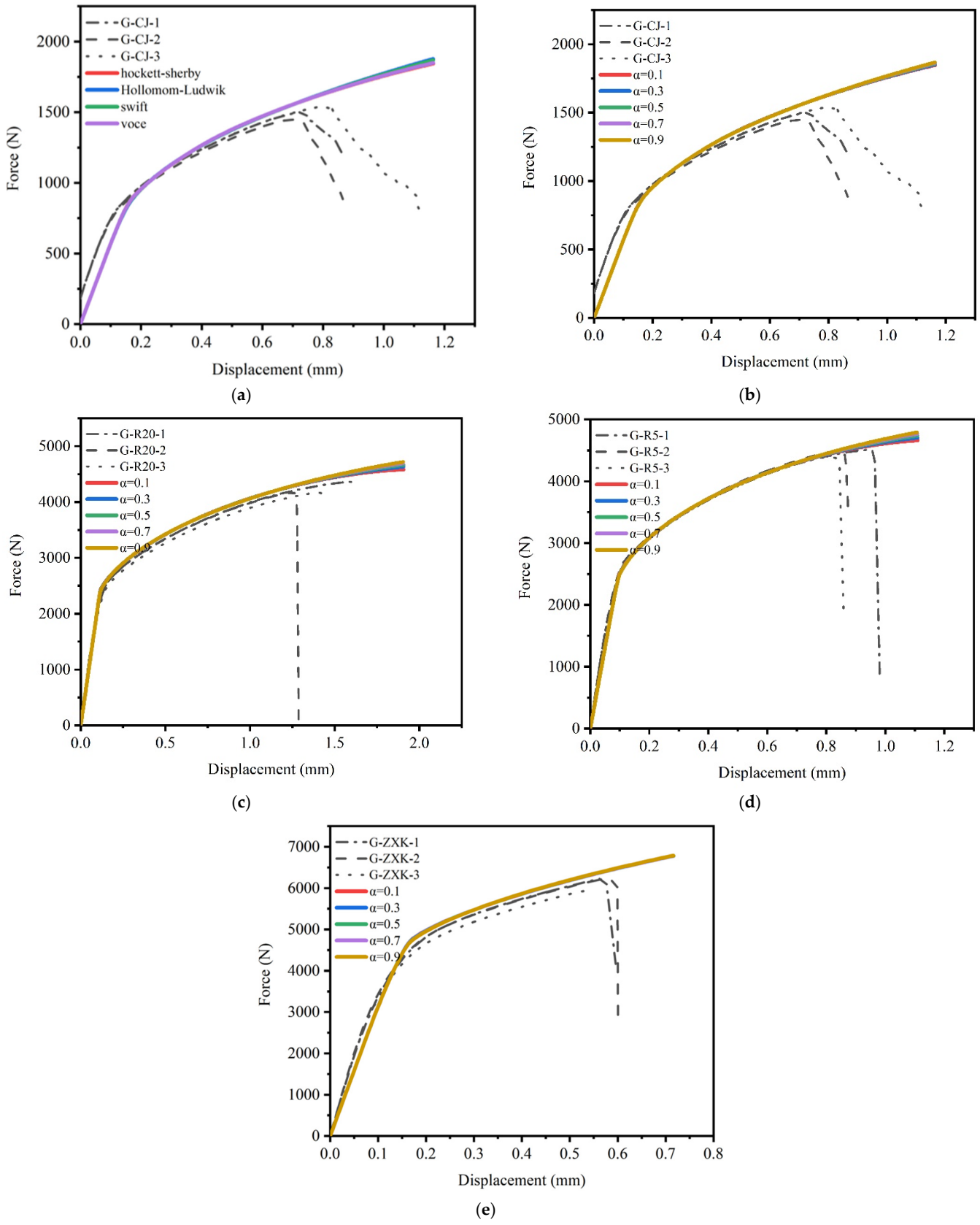

Figure 8. Mixed hardening model with variable weighting coefficients under complex stress states. (**a**) Pure shear test and simulation, (**b**) tension–shear test and simulation, (**c**) R20 specimen test and simulation, (**d**) R5 specimen test and simulation, (**e**) central hole test and simulation.

As shown in Table 4, The predictive accuracy of the present fracture model remains above 93% for all mechanical test conditions, demonstrating stable and reliable overall performance. The uniaxial tension test achieves the highest prediction accuracy, while the pure shear and tension–shear conditions exhibit relatively lower accuracy. With the increase in the weighting coefficient α, the prediction accuracy slightly decreases without significant deterioration. This indicates that the model is insensitive to parametric variation and possesses excellent stability and generalization capability under complex stress states. When the weighting coefficient α is 0.1, the average fitting accuracy of simulated force under complex stress reaches a maximum of 94.78%, which is the optimal result within the tested parameter range. At this weighting coefficient, the force–displacement curve predicted by the model shows the best consistency with the experimental data. The hybrid hardening model can accurately characterize the plastic hardening evolution of the giga casting magnesium alloy under complex quasi-static stress states.

Table 4. Average maximum force accuracy under complex stress with different coefficients.

Test Type	Maximum Force Accuracy (%)				
	Mean Absolute Accuracy (α = 0.1)	**Mean Absolute Accuracy (α = 0.3)**	**Mean Absolute Accuracy (α = 0.5)**	**Mean Absolute Accuracy (α = 0.7)**	**Mean Absolute Accuracy (α = 0.9)**
Pure Shear	90.3	89.98	90.21	90.17	90.13
Tension–Shear	88.55	87.81	88.31	88.2	88.09
Uniaxial Tension	99.69	98.72	99.56	99.42	99.27
R20 Notched Specimen	95.94	94.84	95.55	95.38	95.23
R5 Notched Specimen	98.64	97.19	98.12	97.89	97.69
Central Hole	95.55	95.21	95.47	95.43	95.39
Overall Average Accuracy	94.78 ± 4.47	93.97 ± 4.22	94.54 ± 4.42	94.42 ± 4.38	94.30 ± 4.34

4.3. Study on Dynamic Constitutive Relations

As shown in the high-speed tensile engineering stress–strain curves in Figure 4b, the ultimate tensile strength of cast Mg-7Al-1.5La-1.0Zn magnesium alloy increases with the rise in strain rate, indicating that the strain rate exerts a significant influence on the deformation behavior of this material. The true stress–strain curves at high strain rates displayed in Figure 9 exhibit identical deformation characteristics.

During vehicle crash events, the strain rate can reach 500/s or higher, giving rise to the strain-rate-hardening effect. Strain-rate hardening refers to the phenomenon that the flow resistance of materials rises with increasing strain rate during plastic deformation, which is recognized as a critical hardening mechanism in plastic deformation [31]. Therefore, the influence of high strain rates must be incorporated into the constitutive model. Based on the Swift–Hockett–Sherby mixed hardening constitutive model established in Section 4.1, the effect of strain rate on the constitutive model is investigated, and a dynamic increase factor (DIF) is introduced into Equation (7).

$$\sigma_T = \left\{ \alpha \cdot K\left(\varepsilon_p + \varepsilon_0\right)^n + (1-\alpha) \cdot \left[\sigma_0 + A\left[1 - \exp\left(-b\varepsilon_p^m\right)\right]\right] \right\} * DIF \quad (7)$$

where DIF denotes the dynamic stress amplification factor. In constitutive modeling research, the J-C model and its modified versions [32], as well as the Cowper–Symonds equation [33], are widely adopted to characterize the strain-rate-hardening behavior of metal sheets. In the complete J-C formulation, the equivalent stress is a function of plastic strain, strain rate and temperature. For room-temperature tensile conditions of automotive metal sheets, the temperature term can generally be neglected. The DIF coefficient can

be defined separately based on the modified Johnson–Cook equation and the Cowper–Symonds equation, followed by fitting of relevant material parameters [34].

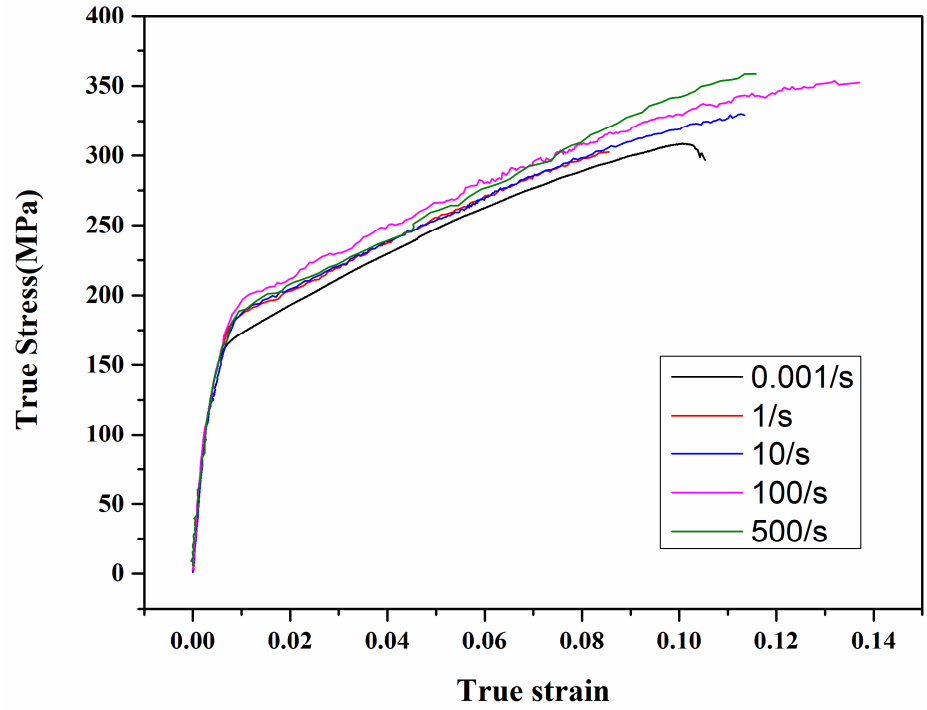

Figure 9. True stress–strain curves under different strain rates.

The proposed dynamic increase factor (DIF) formula is developed based on the strain-rate logarithmic term of the classical Johnson–Cook (J-C) constitutive model. The standard temperature-independent J-C Equation (3) is written as:

$$\overline{\sigma} = \left(A + B\varepsilon_p^n\right) \cdot \left[1 + C\ln\left(\frac{\dot{\varepsilon}}{\dot{\varepsilon}_0}\right)\right] \tag{8}$$

where the dynamic enhancement part $DIF_{J\text{-}C} = 1 + C\ln\left(\frac{\dot{\varepsilon}}{\dot{\varepsilon}_0}\right)$ assumes decoupling between strain hardening and strain-rate hardening, which cannot reflect the coupling interaction between the equivalent plastic strain and strain-rate sensitivity of giga casting magnesium alloys under large crash deformation.

To address this limitation, two modifications are conducted on the original J-C dynamic term:

(1) The constant offset "1" in the J-C DIF is removed, focusing on the strain-rate-induced stress increment during plastic flow.
(2) A power term ε^{p_1} related to equivalent plastic strain is multiplied to couple the cumulative plastic deformation level with the magnitude of strain-rate strengthening.

Finally, the modified DIF expression is obtained:

$$DIF = C\cdot\ln\frac{\dot{\varepsilon}}{\dot{\varepsilon}_0} \cdot \varepsilon^{p_1} \tag{9}$$

In this formula, C inherits the strain-rate coefficient from the J-C model, $\dot{\varepsilon}$ denotes the quasi-static reference strain rate, and p_1 is a newly introduced coupling constant to characterize the influence of plastic strain on strain-rate-hardening behavior. The dynamic flow stress is solved by $\sigma_d = \sigma_s \cdot DIF$, where $\sigma_s = A + B\varepsilon_p^n$ is consistent with the quasi-static hardening part of the J-C model.

The standard temperature-independent Cowper–Symonds Equation (10) is written as:

$$\overline{\sigma} = \left[\left(1 + \frac{\dot{\varepsilon_p}}{C}\right)^{\frac{1}{P}}\right]\sigma_0 \tag{10}$$

The original Cowper–Symonds model only considers the strain-rate-strengthening effect with a constant offset term. To simultaneously describe the coupling effect of strain rate and plastic strain on the dynamic flow stress of giga casting magnesium alloy, a modified Cowper–Symonds dynamic increase factor (DIF), shown in Equation (11), is proposed in this work:

$$DIF = \left(\frac{\dot{\varepsilon}}{C}\right)^{\frac{1}{P}} \cdot P_1 \cdot \varepsilon^{P_2} \tag{11}$$

where DIF denotes the dynamic increase factor; $\dot{\varepsilon}$ is the equivalent plastic strain rate; $\overline{\varepsilon}$ represents the equivalent plastic strain; and C, P, P_1 and P_2 are material fitting constants calibrated from multi-strain-rate tensile test data.

As shown in Table 5, the modified Johnson–Cook equation achieves the best fitting precision for the dynamic increase factor. In the $DIF = C{\cdot}\ln\frac{\dot{\varepsilon}}{\dot{\varepsilon}_0} \cdot \varepsilon^{P_1}$ equation, the fitted material constants are C = 0.064 and P_1 = 50.7925. Analyzed from the perspectives of mathematical formulation and microscopic deformation mechanism, the Johnson–Cook model exhibits higher fitting accuracy than the Cowper–Symonds model under high-strain-rate loading conditions. The Cowper–Symonds model adopts a power-law function to describe strain-rate strengthening, which predicts that flow stress rises steeply and continuously with increasing strain rate. Nevertheless, giga casting magnesium alloys feature a hexagonal close-packed (HCP) crystal structure. Extensive twin activation under high strain rates weakens the strain-rate sensitivity, leading to a gradual slowdown in the growth of flow stress [35]. Accordingly, the power-law expression substantially overestimates the dynamic flow stress. Furthermore, this model fails to capture the coupling between plastic strain and strain-rate strengthening, leading to significant deviations from experimental data under large deformations. In contrast, the logarithmic strain-rate term of the J-C model is consistent with the trend of slowed strain-rate hardening for magnesium alloys at high strain rates. Additionally, a power coupling term related to plastic strain can be introduced on the basis of its intrinsic strain-hardening term to realize bidirectional coupling between cumulative plastic deformation and strain-rate effects. Benefiting from higher fitting degrees of freedom and better compatibility with the twin-dominated plastic deformation mechanism, the modified DIF equation derived from the J-C framework achieves superior agreement with experimental data across the full ranges of strain.

Table 5. Fit of each strain-rate equation.

Strain-Rate Equation	0.001/s	1/s	10/s	100/s	500/s	Average Fitting
Johnson–Cook modified	0.9919	0.9906	0.9887	0.9932	0.9959	0.9921 ± 0.0027
Cowper–Symonds	0.9913	0.9905	0.9803	0.9934	0.9957	0.9902 ± 0.0059

Figure 10 compares the simulated and experimental true stress–strain curves at various strain rates. It can be observed that favorable agreement exists between simulation and experiment under identical strain rates.

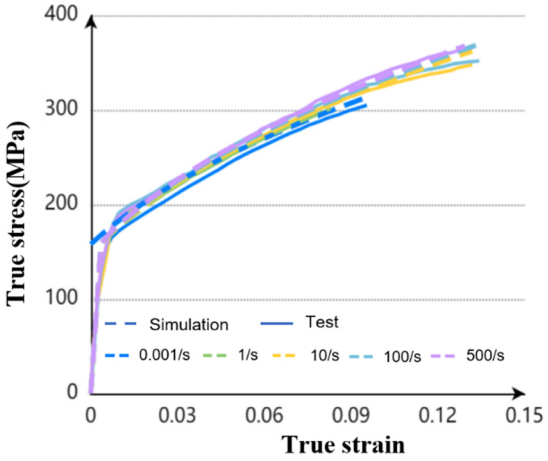

Figure 10. True stress–strain curves: model fitting vs. experiment for multiple strain rates.

4.4. Study on Ductile Fracture Failure Under Complex Stress States

Under extreme dynamic loads such as vehicle collision, magnesium alloy components are not subjected to pure tension or shear stress alone, but operate under complex combined stress states dominated by stress triaxiality and Lode angle [36]. Their fracture failure behavior exhibits a strong dependence on stress states. Traditional failure models with constant failure strain fail to reflect the differences in the plastic deformation and fracture threshold of materials under various stress states, which readily causes defects in simulation results, including delayed fracture, inaccurate crack locations and biased energy absorption prediction.

Based on the continuum damage mechanics theory, this section investigates fracture failure models for complex stress states. By coupling stress state parameters, strain-rate effect and nonlinear damage evolution laws, the whole process of the magnesium alloy from plastic accumulation and damage initiation to macroscopic fracture can be accurately described. Typical fracture models considering the influence of stress states include the J-C model, MMC model and DIEM.

(1) J-C Fracture Model [10,37]

Proposed based on the void growth theory, the J-C fracture model is widely applied to characterize material fracture under plane stress conditions, as expressed in Equation (12). In the formula, D_1, D_2, D_3, D_4 and D_5 are material constants, and $\varepsilon_f\left(\eta, \dot{\varepsilon}, T\right)$ are the variables representing the critical equivalent plastic strain at the fracture of the material under different stress states, strain rates and temperatures

$$\varepsilon_f\left(\eta, \dot{\varepsilon}, T\right) = \left[D_1 + D_2 e^{(D_3\eta)}\right]\left[1 + D_4 \ln\left(\frac{\dot{\varepsilon}_p}{\dot{\varepsilon}_p^{\cdot 0}}\right)\right]\left[1 + D_5\left(\frac{T - T_r}{T_m - T_r}\right)\right] \quad (12)$$

or metallic sheets used in automobiles; the temperature effect is generally neglected, so the J-C fracture model can be simplified, as shown in Equation (13).

$$\varepsilon_f\left(\eta, \dot{\varepsilon}\right) = \left[D_1 + D_2 e^{(D_3\eta)}\right]\left[1 + D_4 \ln\left(\frac{\dot{\varepsilon}_p}{\dot{\varepsilon}_p^{\cdot 0}}\right)\right] \quad (13)$$

In the J-C fracture model, the damage factor D is adopted to determine the failure moment, and its calculation is given by Equation (14). Here, $d\varepsilon_p$ denotes the increment of plastic strain. The material fails and cracks initiate when D = 1.

$$D = \int \frac{d\varepsilon_p}{\varepsilon_f\left(\eta, \dot{\varepsilon}\right)} \tag{14}$$

The J-C fracture model can simultaneously account for the effects of stress state and strain rate on material fracture properties, and delivers high prediction accuracy in regions with high stress triaxiality.

(2) MMC Fracture Model [38]

In 2008, Bai Y and Wierzbicki T [39] proposed the MMC fracture model based on the Mohr–Coulomb fracture mechanism. They replaced the relevant parameters in the original Mohr–Coulomb model with stress triaxiality and Lode angle, as expressed in Equation (15). In the formula, the variable represents the critical equivalent plastic strain at fracture under different stress states, while K, C, f and n are material constants.

$$\varepsilon_f(\eta, \xi) = \left\{ \frac{K}{C}\left[C_\theta^s + \frac{\sqrt{3}}{2-\sqrt{3}}(1 - C_\theta^s)\left(\sec(\frac{\pi\bar{\theta}}{6}) - 1\right)\right]\left[\sqrt{\frac{1+f^2}{3}}\cos(\frac{\pi\bar{\theta}}{6}) + f\left(\eta + \frac{1}{3}\sin(\frac{\pi\bar{\theta}}{6})\right)\right]\right\}^{-\frac{1}{n}} \tag{15}$$

In the MMC fracture model, damage is assumed to accumulate linearly. The defined damage factor D is expressed in Equation (16). The material fails and cracks emerge when D = 1.

$$D = \int \frac{d\varepsilon_p}{\varepsilon_f(\eta, \xi)} \tag{16}$$

The MMC fracture model takes into account the influences of stress triaxiality and Lode angle on material fracture properties, and achieves high prediction accuracy across the full range of stress triaxiality.

(3) DIEM Fracture Model [40]

The DIEM fracture model considers the effect of stress state on material fracture performance, as presented in Equation (17).

$$\varepsilon_f(\eta, \tau_{max}) = e_0 \cdot e^{(-f\theta)} + e_1 \cdot e^{(f\theta)} \tag{17}$$

where $\varepsilon_f(\eta, \tau_{max})$ denotes the critical equivalent plastic strain at damage initiation; η is the stress triaxiality; τ_{max} represents the maximum shear stress; and θ is the normalized Lode angle parameter. e_0, e_1 and f are three material constants calibrated by multiple mechanical tests under different stress states.

In the DIEM fracture model, damage is assumed to accumulate linearly. The damage factor D is defined in Equation (18). The material fails and cracks initiate when D = 1.

$$D = \int \frac{d\varepsilon_p}{\varepsilon_f(\eta, \tau_{max})} \tag{18}$$

The DIEM fracture model accounts for the effect of stress state on material fracture properties and maintains high prediction accuracy over the entire range of stress triaxiality.

Figure 11 compares the simulated force–displacement curves predicted by the J-C, MMC and DIEM fracture models with experimental measurements under six working conditions. A comparative analysis was conducted on the fracture prediction accuracy of the J-C, MMC and DIEM for magnesium alloys under complex stress conditions.

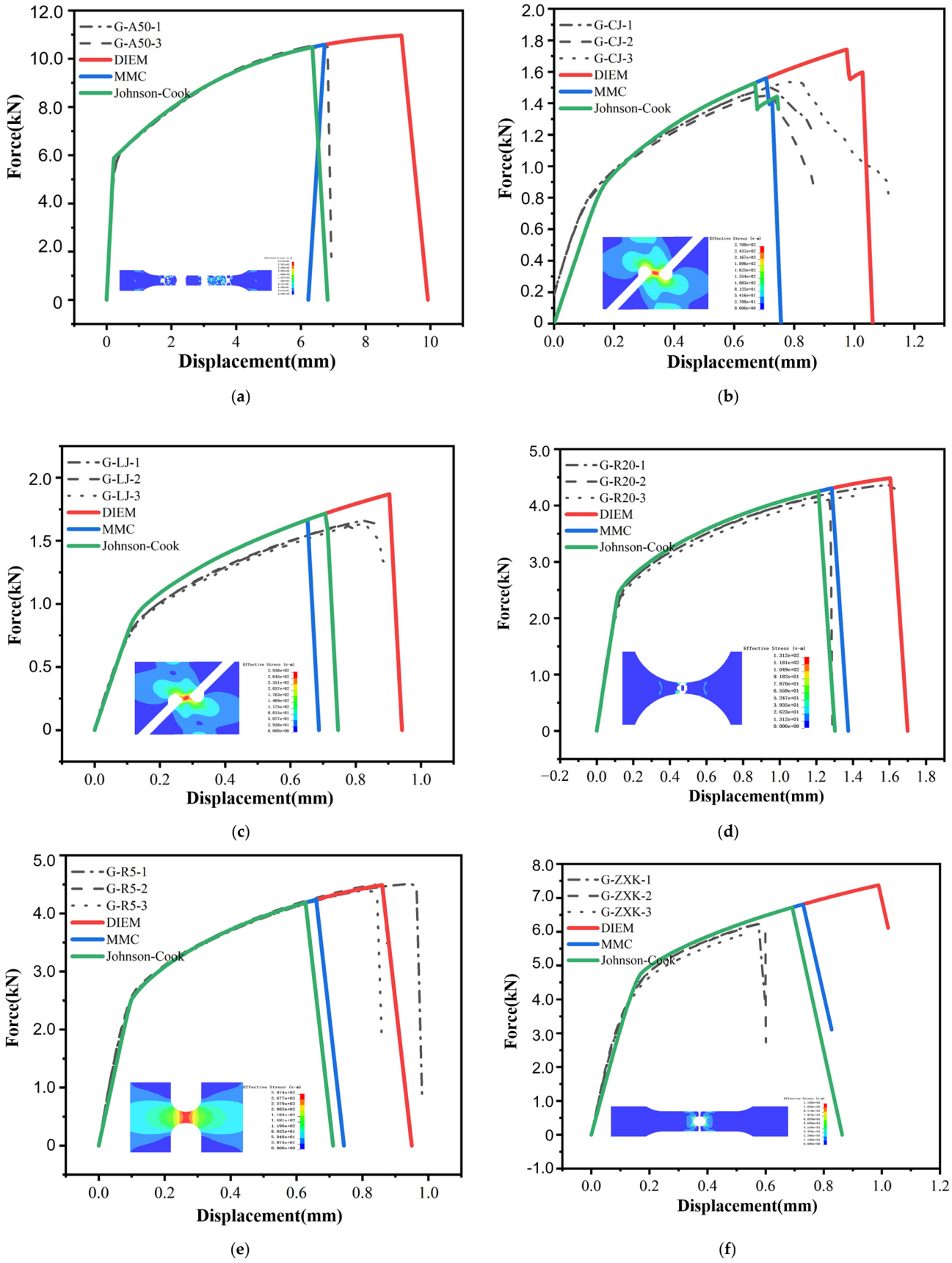

Figure 11. Comparison between simulation and test results of different fracture failure models under complex stress states. (**a**) Uniaxial tension: simulation vs. test; (**b**) pure shear: simulation vs. test; (**c**) tension–shear: simulation vs. test; (**d**) R20: simulation vs. test; (**e**) R5: simulation vs. test; (**f**) central hole: simulation vs. test.

Table 6 summarizes the mean absolute prediction accuracy of fracture displacement for three fracture constitutive models, namely Johnson–Cook (J-C), MMC and DIEM, for six specimens with distinct stress states: pure shear, tension–shear, uniaxial tension, R20 notched specimen, R5 notched specimen and central hole specimen. The overall average accuracy and corresponding standard deviation across all loading cases are calculated to quantitatively evaluate the prediction accuracy and stability of the three models under various stress triaxiality conditions.

Table 6. Fracture displacement accuracy of different fracture failure models under complex stress states.

Test Type	Fracture Displacement Accuracy (%)		
	Mean Absolute Accuracy (J-C Model)	Mean Absolute Accuracy (MMC Model)	Mean Absolute Accuracy (DIEM)
Pure Shear	89.86	94.71	69.14
Tension–Shear	87.22	80.52	88.55
Uniaxial Tension	95.95	97.37	96.10
R20 Notched Specimen	86.60	90.06	85.43
R5 Notched Specimen	72.82	81.51	94.35
Central Hole	76.29	74.56	23.16
Overall Average Accuracy	84.79 ± 8.66	86.46 ± 8.96	76.1 ± 27.66

All three models achieve optimal prediction performance under uniaxial tension: the accuracy of the J-C model reaches 95.95%, the MMC model 97.37%, and the DIEM 96.10%. All values exceed 95%, demonstrating that the three models can well characterize the fracture behavior under simple uniaxial tension, among which the MMC model delivers the highest prediction accuracy for uniaxial tension.

The MMC model exhibits remarkable superiority under pure shear loading, with a prediction accuracy of 94.71%, far exceeding the J-C model (89.86%) and the DIEM (69.14%). This indicates that the DIEM fails to accurately describe fracture displacement under pure shear conditions.

Obvious discrepancies are observed for R5 notched specimens: the DIEM achieves an accuracy of 94.35%, which is substantially higher than the MMC model (81.51%) and the J-C model (72.82%). This reveals that the DIEM has better adaptability for notched specimens under high stress triaxiality. However, the DIEM only attains an accuracy of 23.16% for central hole specimens, leading to invalid predictions and far inferior performance compared with the other two models. This manifests as the DIEM possessing extremely poor adaptability to diverse loading cases and only being valid for specific notched specimens with high stress triaxiality.

For tension–shear and R20 notched specimens (two cases with moderate stress triaxiality), the MMC model maintains a moderately high and stable prediction level without extremely high or low errors.

The overall average prediction accuracy over the six test cases follows the order: MMC model (86.46%) > J-C model (84.79%) > DIEM (76.10%). In terms of overall average accuracy alone, the MMC model provides the best overall predictive capability for fracture displacement under multiple stress states, followed by the J-C model, while the DIEM yields the lowest overall average accuracy.

Figure 12 illustrates the variation in equivalent plastic strain at fracture with stress triaxiality for the three fracture models. The fracture strain of the J-C model decreases linearly as stress triaxiality rises; the MMC model presents a flat curve with generally low fracture strain and negligible variation range; the DIEM shows distinct characteristics,

with obvious peaks and troughs within the negative triaxiality range and drastic curve fluctuations. Although the DIEM fully reproduces the evolution of fracture strain across wide stress triaxiality and the J-C model reflects the linear attenuation of ductility, the MMC model achieves the highest accuracy in peak force prediction. The MMC model predicts lower critical fracture strain under moderate triaxial tension, triggering material failure in advance and matching experimental peak load well. By contrast, DIEM and J-C overestimate plastic deformation before fracture, leading to overpredicted maximum force in simulations.

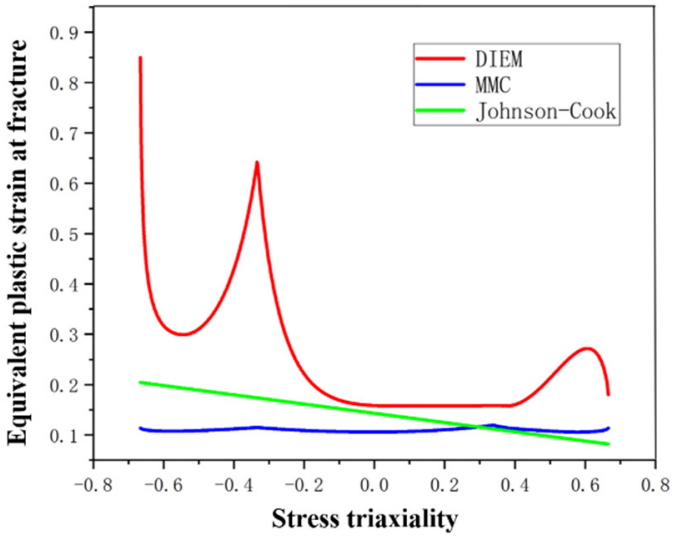

Figure 12. Stress triaxiality versus fracture equivalent plastic strain curves of three fracture models.

The MMC model theoretically establishes a quantitative correlation between stress state and fracture strain. Its parameters need to be calibrated via multiple tests including pure shear, notched and central holed specimens, making it applicable to failure prediction of giga casting magnesium alloy components under complex loads. The calibrated parameters of the MMC fracture model are listed in Table 7.

Table 7. Parameters of MMC fracture model.

Parameter	K	C	C_{θ}^{s}	f	n
Value	651	162	0.8700	0.1034	0.3527

In crash simulation calculations [41], mesh size exerts a remarkable influence on the accuracy of fracture prediction. Coarse elements fail to capture local necking and high strain gradients, which leads to delayed fracture prediction or non-conservative results. In contrast, excessively fine elements greatly increase computational cost. Mesh sensitivity analysis can establish a scaling function between failure strain and element size to stabilize energy dissipation and obtain mesh-independent numerical results.

In this work, five mesh sizes ranging from 0.5 mm to 6 mm are selected for mesh effect and convergence analysis, namely 0.5 mm, 1.0 mm, 2.0 mm, 4.0 mm and 6.0 mm. Uniaxial tensile finite element simulations are performed via LS-DYNA. Multi-scale mesh models are constructed to calculate load responses and output force–displacement curves, as presented in Figure 13.

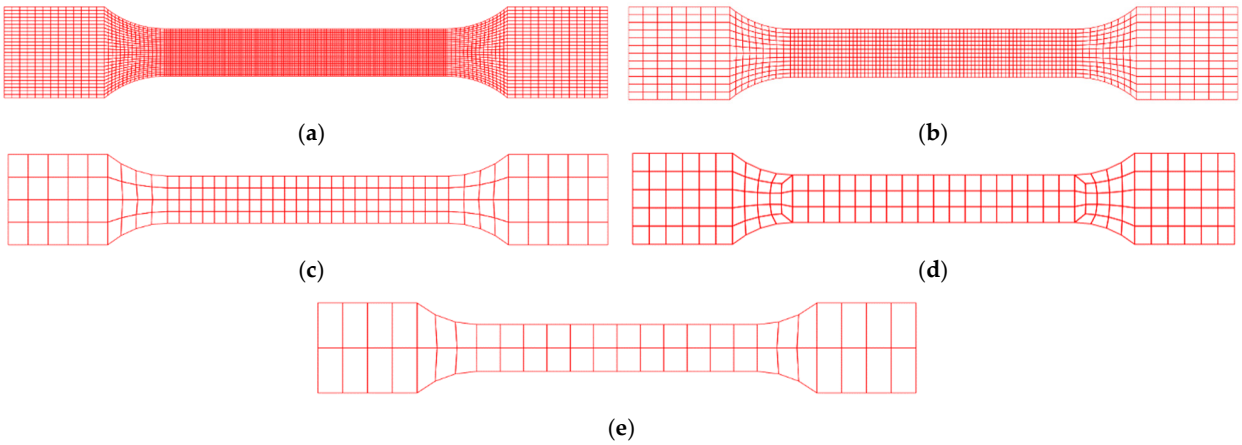

Figure 13. Uniaxial tensile finite element models under various mesh dimensions: (**a**) 0.5 mm, (**b**) 1.0 mm, (**c**) 2.0 mm, (**d**) 4.0 mm, (**e**) 6.0 mm.

As shown in Equation (19), the convergence order p characterizes the decay rate of finite element discretization error, and r denotes the mesh refinement ratio, which is defined as the ratio of coarse mesh size to fine mesh size.

$$p = \frac{\ln\left(\left|\frac{f_{i+1}-f_i}{f_i-f_{i-1}}\right|\right)}{\ln(r)} \tag{19}$$

Equation (15) defines the Grid Convergence Index (GCI) for quantifying mesh-caused discretization error from multi-mesh computation; lower GCI means better mesh independence. The safety factor Fs for three mesh cases is taken as 1.25.

$$GCI_{fine} = \frac{F_s \cdot \left|Error_{(i,i+1)}\right|}{r_{(i,i+1)}^{p} - 1} \tag{20}$$

Figure 14a presents the force–displacement curves obtained from simulations with models of different mesh sizes. The curves show favorable consistency in both elastic and plastic stages, while discrepancies emerge during the necking stage. The peak force values are extracted and plotted against mesh size in Figure 14b. The peak forces of adjacent mesh sizes differ slightly and fluctuate around 10,400 N. When the mesh size decreases from 6 mm to 0.5 mm, the peak force only rises by 35.19 N.

As listed in Table 8, according to the analysis of force–displacement curves for different mesh sizes, the variation in peak force between adjacent mesh dimensions is merely 0.187%. The calculated convergence order p reaches a maximum value of 1.64, less than 2. The Grid Convergence Index (GCI) is further calculated via Equation (15): GCI (0.5, 1.0) = 0.013%, GCI (1.0, 2.0) = 0.020%, and GCI (2.0, 4.0) = 0.163%. These results demonstrate satisfactory mesh convergence, and the constitutive and fracture parameters derived from the present mesh scheme are reliable for reference.

Table 8. Analysis of force–displacement curves with various mesh sizes.

Mesh Size h (mm)	Max Force (N)	Absolute Percentage Difference in Maximum Force	P	GCI
0.5	10,407.33	-	-	-
1.0	10,406.85	0.014%	1.23	0.013%
2.0	10,403.38	0.033%	1.64	0.020%
4.0	10,392.57	0.104%	1.05	0.163%
6.0	10,373.16	0.187%	-	-

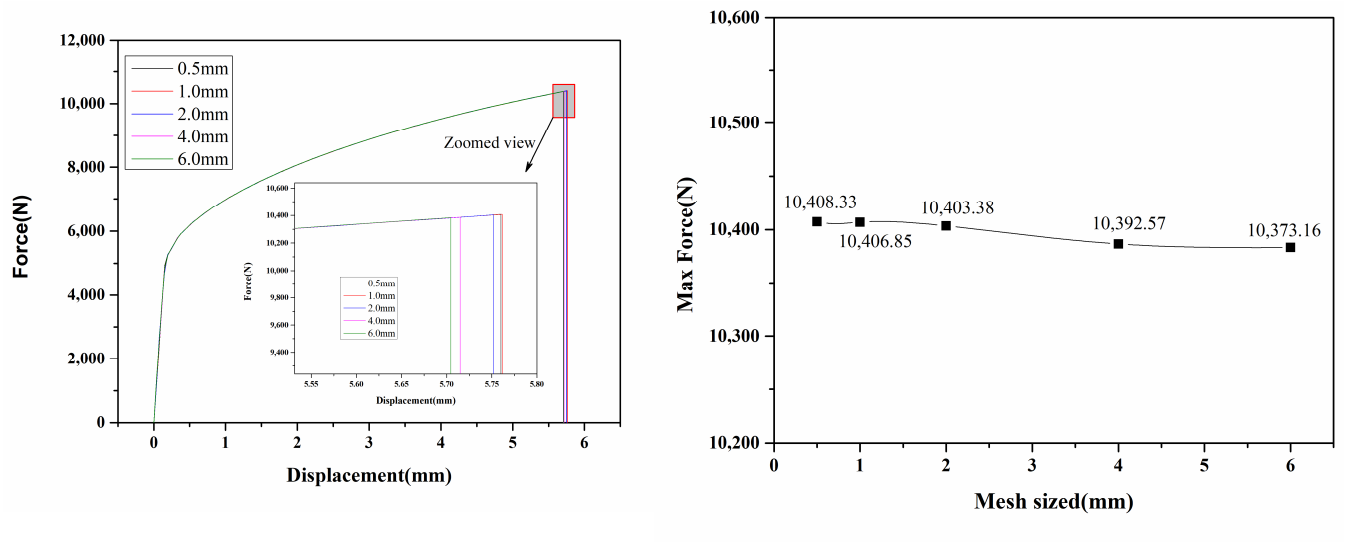

(**a**) (**b**)

Figure 14. Force–displacement curves from simulations with various mesh dimensions. (**a**) Force–displacement curves; (**b**) max force under various mesh dimensions.

4.5. Microstructure Analysis of Cast Magnesium Alloys

Figure 15 presents the optical microstructure of giga casting Mg-7Al-1.5La-1.0Zn alloy. No severe casting defects such as obvious porosity, cracks or large inclusions are observed; only tiny amounts of microporosity exist, which conforms to the typical microstructural characteristics of die casting alloys. The material exhibits typical fine-grained features of die casting, with dense and uniform α-Mg solid solution matrix. Rapid solidification during high-pressure die casting significantly refines grains and suppresses the formation of coarse dendrites. Scanning electron microscopy further reveals that intergranular second phases are discretely distributed as short rods and fine particles with regular morphology and low agglomeration. Combined with alloy composition, these phases include β-$Mg_{17}Al_{12}$ and rare-earth $Al_{11}La_3$. The addition of La alleviates segregation and coarsening of second phases. Uniformly dispersed grain boundary phases exert strong pinning effects to restrain grain growth and dislocation slip, improving microstructural stability and laying a sound microstructural foundation for excellent mechanical and fracture performance. EDS analysis verifies that the second phases are rich in Al, La and Zn, corresponding to Al-Mg-La rare-earth intermetallic compounds.

As shown in Figure 16, X-ray diffraction (XRD) tests were performed on high-pressure die casting Mg-7Al-1.5La-1.0Zn alloy specimens, and full-spectrum phase identification was completed by matching standard PDF cards. All major diffraction peaks correspond to the hexagonal close-packed (HCP) α-Mg matrix with typical characteristic peaks of magnesium substrate. The sharp peak shapes without obvious broadening demonstrate the favorable crystallinity of the die casting matrix.

Characteristic diffraction peaks of β-$Mg_{17}Al_{12}$ are detected in the spectrum, which is a conventional intermetallic compound precipitated via a eutectic reaction between the Al and Mg matrix. Meanwhile, diffraction peaks of rare-earth intermetallics $Al_{11}La_3$ and Al_3La are identified, verifying that La participates in forming novel rare-earth second phases. No independent diffraction peaks of elemental Al, La or Zn are observed; Zn is mainly dissolved in the α-Mg matrix and rare-earth phases.

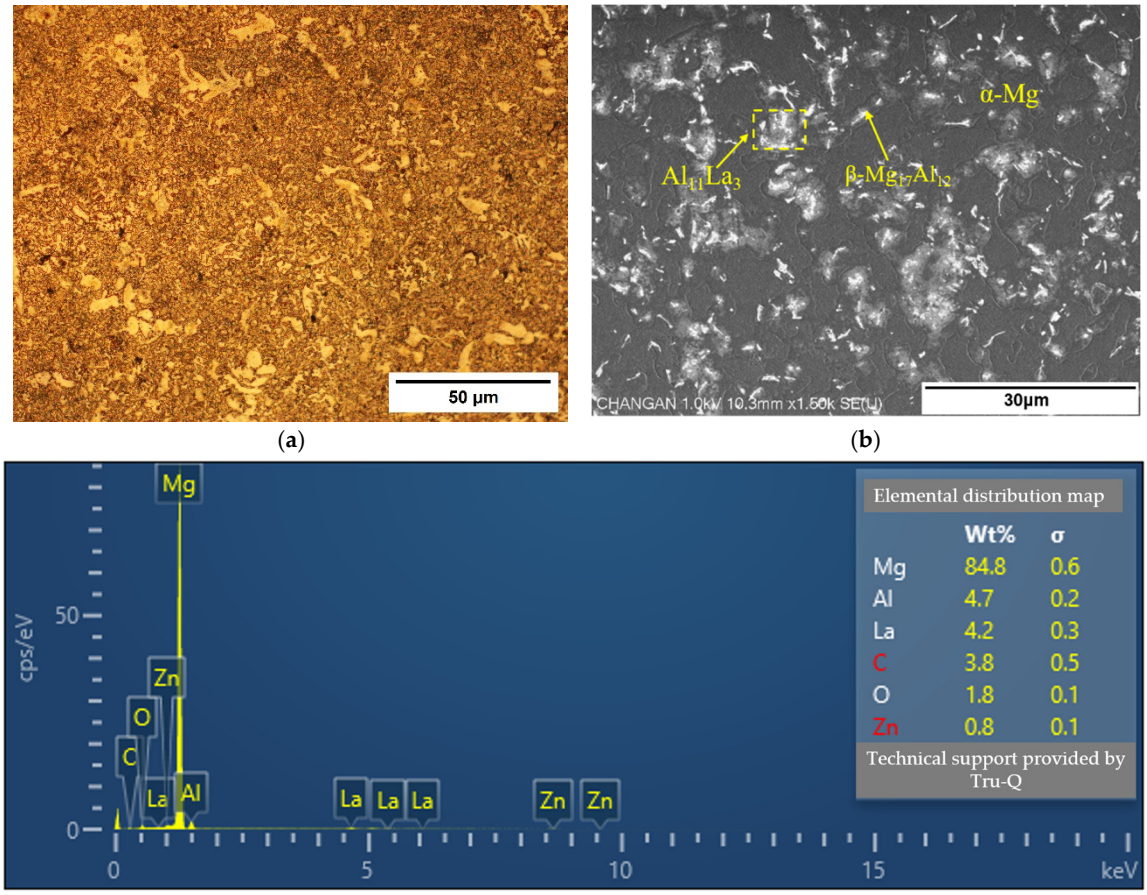

Figure 15. Microstructure of Mg-7Al-1.5La alloy. (**a**) Optical micrographs of HPDC Mg-7Al-1.5La alloys, (**b**) SEM of HPDC Mg-7Al-1.5La alloys, (**c**) EDS scanning spectra of local regions in Mg-7Al-1.5La alloy.

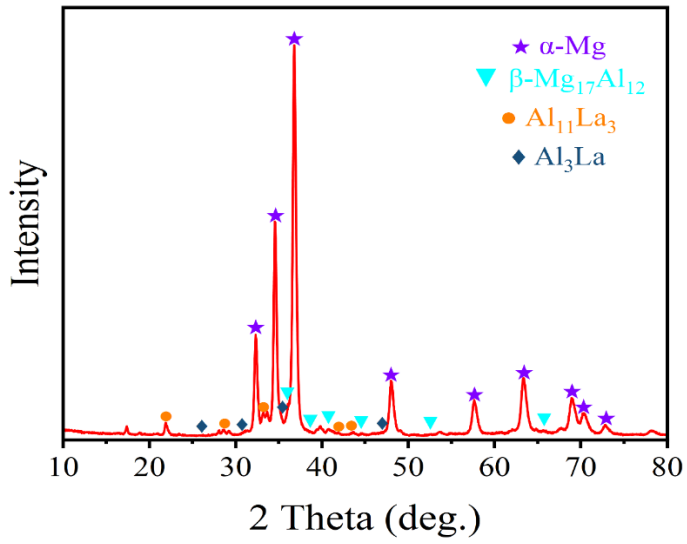

Figure 16. XRD pattern of high-pressure die casting Mg-7Al-1.5La-1.0Zn alloy.

Comparisons of peak intensities indicate that the diffraction intensity of rare-earth intermetallics is comparable to that of β-$Mg_{17}Al_{12}$, revealing equivalent precipitation amounts of the Mg-Al eutectic phase and rare-earth phase. The formation of rare-

earth phases breaks the continuous brittle network of $Mg_{17}Al_{12}$ and optimizes grain boundary properties.

Figure 17a displays the fracture morphology at a tensile strain rate of 0.001 s^{-1}. A large number of dimples are distributed on the fracture surface, and second-phase particles can be observed at the center of some dimples, showing typical characteristics of dimple-coalescence ductile fracture. Figure 17b shows the fracture morphology under a tensile strain rate of 0.1 s^{-1}. Abundant dimples can also be found on the specimen, along with fragmented second-phase particles in local regions. Figure 17c corresponds to the tensile strain rate of 10 s^{-1}. Fragmented second-phase particles are widely distributed on the fracture surface, and the material exhibits a ductile–brittle mixed fracture mode. Figure 17d presents the fracture morphology tested at a tensile strain rate of 500 s^{-1}, where the failure occurs via an evident mixed fracture mode combining intergranular fracture and transgranular cleavage [42]. Rapid cooling during high-pressure die casting combined with La rare-earth elements synergistically refines the α-Mg matrix grains. Grain refinement drastically increases the critical stress required for transgranular cleavage. Meanwhile, the rare-earth addition eliminates the strong basal texture typical of wrought magnesium alloys, resulting in randomly distributed grain orientations. Few grains contain large continuous parallel basal planes, which inhibits the formation of extensive river patterns. After La is incorporated, thermally stable and dispersed $Al_{11}La_3$ rare-earth secondary phases form, replacing the continuous brittle intermetallic network. These hard rare-earth particles tend to fragment preferentially under high strain, generating microvoids along grain boundaries.

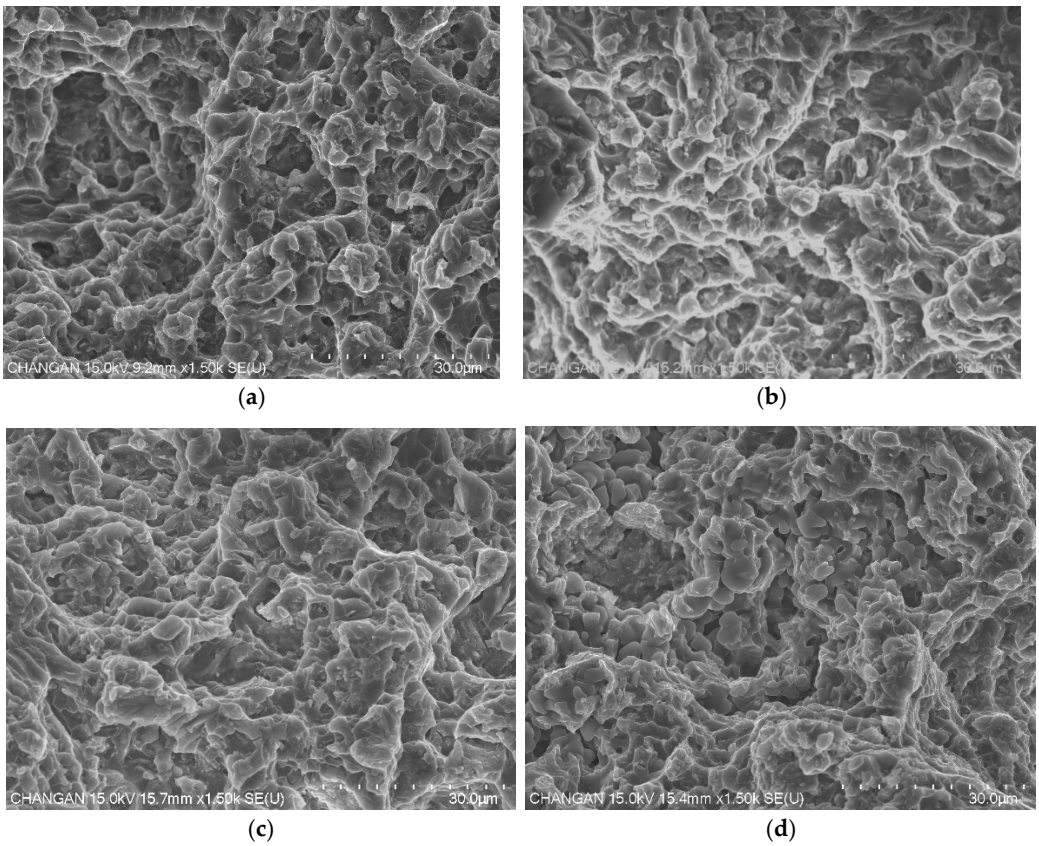

Figure 17. Fracture morphologies under different strain rates. (**a**) Strain rate 0.001/s, (**b**) strain rate 0.1/s, (**c**) strain rate 10/s, (**d**) strain rate 500/s.

5. Conclusions

When magnesium alloys are applied to automotive structural components, they are generally subjected to complex combined tension–compression and shear stress during

vehicle crashes. Research on numerical constitutive models for crashworthiness simulation remains limited, which restricts the wider application of magnesium alloys in load-bearing parts. Targeting automotive crash conditions, this study investigated the plastic constitutive equation of the giga casting Mg-7Al-1.5La-1Zn magnesium alloy under complex stress states, and proposed a novel plastic constitutive equation suitable for automotive magnesium alloys. Furthermore, the prediction accuracy of three fracture models for the fracture behavior of giga casting magnesium alloys was compared via simulation and experimental verification.

The main conclusions are summarized as follows:

(1) For the die casting Mg-7Al-1.5La-1Zn magnesium alloy, a mixed hardening model $\sigma = a \cdot \text{Swift} + (1 - a) \cdot \text{Hockett} - \text{Sherby}$ was adopted under uniaxial stress. When the weighting coefficient α was set to 0.3, the average fitting accuracy of simulated force reached the maximum value of 99.71%. This high accuracy indicates that the flow-hardening behavior of the studied giga casting magnesium alloy during loading is consistent with the characteristics of the saturation hardening model.

(2) Mechanical property tests under five distinct stress states were carried out on die casting Mg-7Al-1.5La-1Zn magnesium alloy. Combined with experimental data and the isotropic constitutive model, the average force fitting accuracy of simulations under complex stress states reaches a peak value of 94.78% when the weighting coefficient α is set to 0.1. Based on the mixed hardening model, a dynamic increase factor is introduced to describe the strain-rate-strengthening effect. Finally, a modified constitutive model is established on the basis of the J-C model.

(3) The fracture prediction performance of the J-C, MMC and DIEM was evaluated for magnesium alloys under complex stress conditions. The prediction accuracy of fracture displacement ranked in descending order, MMC > J-C > DIEM, and the maximum accuracy of the MMC model was 86.46%. The results reveal that the MMC model incorporates stress triaxiality and Lode angle, covering the full stress range from pure shear to high tensile stress. It provides a comprehensive description of ductile fracture under multiaxial stress and is applicable to failure analysis of notched and holed specimens.

In this work, high-precision constitutive and fracture failure models for magnesium alloys were developed, which effectively improved the prediction accuracy of component deformation, crack initiation and energy response in crash simulation. This study provides solid theoretical support and engineering reference for accurate material card modeling and crashworthiness optimization of lightweight magnesium alloy structural parts.

Author Contributions: Conceptualization, S.L.; Methodology, J.Z. (Jinsheng Zhang) and G.H.; Software, Y.J., J.Z. (Jie Zhang) and B.L.; Validation, J.Y.; Formal analysis, Y.W. and Q.Y.; Investigation, J.Z. (Jie Zhang) and P.C.; Resources, G.H. and Q.Y.; Data curation, Y.J., J.Z. (Jie Zhang), P.C., J.Y., Y.W. and B.L.; Writing—original draft, J.Z. (Jinsheng Zhang); Writing—review and editing, J.Z. (Jinsheng Zhang) and G.H.; Visualization, S.L.; Project administration, B.L.; Funding acquisition, G.H. and S.L. All authors have read and agreed to the published version of the manuscript.

Funding: This research was funded by the Special Fund for Technological Innovation and Development of Chongqing (grant numbers CSTB2024TIAD-KPX0001).

Data Availability Statement: The original contributions presented in this study are included in the article. Further inquiries can be directed to the corresponding authors.

Conflicts of Interest: Jinsheng Zhang, Sha Lan, Jie Zhang, Ping Chen, Yazhou Jiang, Yunyun Wang, and Qin Yang were employed Global R&D Center, Chongqing Changan Automobile Co., Ltd., Chongqing 401120, China. The remaining authors declare that the research was conducted in the

absence of any commercial or financial relationships that could be construed as a potential conflict of interest.

References

1. Wang, Y.; Ma, Q.; Wang, T.; Zhang, B.; Wang, D.; Zhang, X.; Nagaumi, H.; Yang, B.; Ren, X.; Huang, J.; et al. Vehicle lightweighting for carbon neutrality: Decarbonization mechanisms, key processes and engineering applications. *Carbon Neutr. Syst.* **2026**, *2*, 2–32. [CrossRef]
2. Del Pero, F.; Berzi, L.; Antonacci, A.; Delogu, M. Automotive Lightweight Design: Simulation Modeling of Mass-Related Consumption for Electric Vehicles. *Machines* **2020**, *8*, 51. [CrossRef]
3. Luo, A.A. Magnesium is at a crossroads: An industrial metal or a technology metal. *J. Magnes. Alloys* **2025**, *13*, 1–3. [CrossRef]
4. Li, T.; Song, J.; Zhang, A.; You, G.; Yang, Y.; Jiang, B.; Qin, X.; Xu, C.; Pan, F. Progress and prospects in Mg-alloy super-sized high pressure die casting for automotive structural components. *J. Magnes. Alloys* **2023**, *11*, 4166–4180. [CrossRef]
5. Logan, S. A Lightweight Automobile Body Concept Featuring Ultra-Large, Thin-Wall Structural Magnesium Castings. In *Essential Readings in Magnesium Technology*; Springer: Cham, Switzerland, 2007; pp. 55–63.
6. Zhang, W.; Xu, J. Advanced lightweight materials for Automobiles: A review. *Mater. Des.* **2022**, *221*, 110994. [CrossRef]
7. Liu, B.; Yang, J.; Zhang, X.; Yang, Q.; Zhang, J.; Li, X. Development and application of magnesium alloy parts for automotive OEMs: A review. *J. Magnes. Alloys* **2023**, *11*, 15–47. [CrossRef]
8. Zhan, L.; Sun, Y.M.; Song, Y.; Kong, C.H.; Ma, K.; Dong, B.X.; Yang, H.Y.; Shu, S.L.; Qiu, F. Thin-walled and large-sized magnesium alloy die castings for passenger car cockpit: Application, materials, and manufacture. *China Foundry* **2024**, *21*, 525–545. [CrossRef]
9. Farrokhnejad, M.; Weiler, J.P.; Zhang, J.; Mao, M.; Cheng, L.; Liu, C.; Li, Z. High pressure die casting (HPDC) tool design & process considerations for a mega-sized magnesium lift gate. *J. Magnes. Alloys* **2026**, *16*, 101982. [CrossRef]
10. Johnson, G.R.; Cook, W.H. Fracture characteristics of three metals subjected to various strains, strain rates, temperatures, and pressures. *Eng. Fract. Mech.* **1985**, *21*, 31–48. [CrossRef]
11. Bai, Y.; Wierzbicki, T. Application of extended Mohr-Coulomb criterion to ductile fracture. *Int. J. Fract.* **2010**, *161*, 1–20. [CrossRef]
12. Helmut, O.G.; Dell, H.G. MF GenYld + CrachFEM. 4.2 User's Manual. 2014. Available online: https://www.matfem.de/crachfem.html (accessed on 18 March 2026).
13. Chen, X.R.; Liao, Q.Y.; Niu, Y.X.; Jia, W.T.; Le, Q.C.; Cheng, C.L.; Yu, F.X.; Cui, J.Z. A constitutive relation of AZ80 magnesium alloy during hot deformation based on Arrhenius and Johnson-Cook model. *J. Mater. Res. Technol.* **2019**, *8*, 1859–1869. [CrossRef]
14. Mirza, F.A.; Chen, D.L.; Li, D.J.; Zeng, X.Q. A modified Johnson-Cook constitutive relationship for a rare-earth containing magnesium alloy. *J. Rare Earths* **2013**, *31*, 1202–1207. [CrossRef]
15. Li, Z.; Wang, J.; Yang, H.; Liu, J.; Ji, C. A Modified Johnson-Cook Constitutive Model for Characterizing the Hardening Behavior of Typical Magnesium Alloys under Tension at Different Strain Rates: Experiment and Simulation. *J. Mater. Eng. Perform.* **2020**, *29*, 8319–8330. [CrossRef]
16. Chang, X.; Zhang, L.; Yang, Y.; Ren, J. Constitutive Models for Compressive Deformation of AZ80 Magnesium Alloy under Multiple Loading Directions and Strain Rates. *J. Iron Steel Res. Int.* **2016**, *23*, 64–68. [CrossRef]
17. Solanki, K.; Williams, C.L.; Darling, K.A. A Review of the Anomalous Dynamic Behavior in Magnesium Alloys. *J. Miner. Met. Mater. Soc.* **2024**, *76*, 1594–1608. [CrossRef]
18. Alhalaybeh, T.S.; Chowdhury, A.I.; Akhtar, H.; Lou, Y. Ductile Fracture Prediction in Mg-ZM51M Alloy Using Inverse-Calibrated Damage Models. *Metals* **2025**, *15*, 722. [CrossRef]
19. Liu, Z.; Zheng, X.; Li, H.; Tian, Y.; Chen, L. Modification of Johnson-Cook Constitutive Equation and Stamping Finite Element Simulation of AM60 Magnesium Alloy. *Mater. Mech. Eng.* **2023**, *47*, 85–91.
20. Yang, Q.; Jiang, B.; Gao, L.; Gao, Y.; Liang, B.; Lan, S.; Qin, Z.; Zou, W.; Yang, F.; Pan, F. Study on Plastic Constitutive Relation and Ductile Fracture Criterion of AM60B Magnesium Alloy. *Materials* **2024**, *17*, 1684. [CrossRef] [PubMed]
21. Wang, Z.; Xing, Z.; Lei, Y.; Hu, B.; Hu, J.; Li, H.; Feng, X.; Kang, G. A review on cyclic plasticity, damage, and fatigue failure of magnesium alloys. *J. Mater. Sci. Technol.* **2025**, *234*, 246–283. [CrossRef]
22. DiCecco, S.; Altenhof, W.; Hu, H. FE Modelling of Tensile and Impact Behaviours of Squeeze Cast Magnesium Alloy AM60. In *Magnesium Technology 2013*; Hort, N., Mathaudhu, S.N., Neelameggham, N.R., Alderman, M., Eds.; Springer: Cham, Switzerland, 2013; pp. 35–39.
23. Khademi, M.; Mirnia, M.J.; Naeini, H.M. Numerical analysis of ductile fracture in stretch bending of AA6061-T6 aluminum alloy sheet using GTN damage model. *Int. J. Solids Struct.* **2024**, *301*, 1129477. [CrossRef]
24. *GB/T228*; Metallic Materials—Tensile Testing at Ambient Temperature. General Administration of Quality Supervision. Inspection and Epidemic of the People's Republic of China: Beijing, China, 2002.
25. *ISO 26203-2:2011*; Metallic Materials—Tensile Testing at High Strain Rates—Part 2: Servo-Hydraulic and Other Test Systems. ISO: Geneva, Switzerland, 2011.

26. Ponnusamy, B. High-fidelity numerical framework for crashworthiness evaluation of passenger car body structures under full-frontal impact. *Sci. Rep.* **2026**, *16*, 10563. [CrossRef] [PubMed]
27. Fereshteh-Saniee, F.; Barati, F.; Badnava, H.; Nejad, K.F. An exponential material model for prediction of the flow curves of several AZ series magnesium alloys in tension and compression. *Mater. Des.* **2012**, *35*, 1–11. [CrossRef]
28. Tu, S.; Ren, X.; He, J.; Zhang, Z. Stress-strain curves of metallic materials and post-necking strain hardening characterization: A review. *Fatigue Fract. Eng. Mater. Struct.* **2020**, *43*, 3–19.
29. Kleemola, H.J.; Nieminen, M.A. On the strain-hardening parameters of metals. *Metall. Trans.* **1974**, *5*, 1863–1866. [CrossRef]
30. Chowdhury, A.I.; Alhalaybeh, T.S.; Zhou, L.; Liang, X.; Lou, Y. Inverse engineering based analytical and numerical prediction on ductile fracture for AZ60M magnesium alloy under wide stress triaxiality. *Eng. Fract. Mech.* **2025**, *326*, 111384. [CrossRef]
31. Straffelini, G. *Ductility and Formability of Metals: A Metallurgical Engineering Perspective*, 1st ed.; Elsevier: Amsterdam, The Netherlands, 2023.
32. Johnson, G.R.; Cook, W.H. A constitutive model and data for metals subjected to large strains, high strain rates and high temperatures. In *Proceedings of the 7th International Symposium on Ballistics, International Ballistics Committee, The Hague, The Netherlands, 19–21 April 1983*; American Defense Preparedness Association: Arlington, VA, USA, 1983; pp. 541–547.
33. Cowper, G.R.; Symonds, P.S. Strain-hardening and strain rate effects in the impact loading of cantilever beams. *Brown Univ. Appl. Math. Rep.* **1958**, *28*, 1–46.
34. Al Salahi, A.A.; Othman, R. Constitutive Equations of Yield Stress Sensitivity to Strain Rate of Metals: A Comparative Study. *J. Eng.* **2016**, *2016*, 3279047. [CrossRef]
35. Guo, P.; Li, L.; Liu, X.; Ye, T.; Cao, S.; Xu, C.; Li, S. Compressive deformation behavior and microstructure evolution of AM80 magnesium alloy under quasi-static and dynamic loading. *Int. J. Impact Eng.* **2017**, *109*, 112–120. [CrossRef]
36. Deng, Y.; Hu, A.; Xiao, X.; Jia, B. Experimental and numerical investigation on the ballistic resistance of ZK61m magnesium alloy plates struck by blunt and ogival projectiles. *Int. J. Impact Eng.* **2021**, *158*, 104021. [CrossRef]
37. Mareau, C. A thermodynamically consistent formulation of the Johnson–Cook model. *Mech. Mater.* **2020**, *143*, 103340. [CrossRef]
38. Dunand, M.; Mohr, D. On the predictive capabilities of the shear modified Gurson and the modified Mohr-Coulomb fracture models over a wide range of stress triaxialities and Lode angles. *J. Mech. Phys. Solids* **2011**, *59*, 1374–1394. [CrossRef]
39. Bai, Y.; Wierzbicki, T. A new model of metal plasticity and fracture with pressure and Lode dependence. *Int. J. Plast.* **2008**, *24*, 1071–1096. [CrossRef]
40. Andrade, F.X.C.; Feucht, M.; Haufe, A. On the prediction of material failure in LS-DYNA: A comparison between GISSMO and DIEM. In Proceedings of the 13th International LS-DYNA Conference, Detroit, MI, USA, 4–5 June 2014.
41. Wang, J.J.; Li, J.; Meng, D.W. Impact test for calculating failure strain of steel box. *J. Archit. Civ. Eng.* **2014**, *31*, 28–35.
42. Zhi, H.D.; Guo, B.Q.; Ding, N.; Yan, Z.; Zhu, J.; Wan, C. Johnson-Cook constitutive model and failure parameters of Mg-9Gd-4Y-2Zn-0.5Zr alloy. *Rare Met. Mater. Eng.* **2025**, *54*, 714–721.

Disclaimer/Publisher's Note: The statements, opinions and data contained in all publications are solely those of the individual author(s) and contributor(s) and not of MDPI and/or the editor(s). MDPI and/or the editor(s) disclaim responsibility for any injury to people or property resulting from any ideas, methods, instructions or products referred to in the content.